energies

MDPI

Article

Research on High-Performance Speed Regulation of Switched Reluctance Motor Based on Improved Nonsingular Fast Terminal Sliding Mode Control and an Adaptive Bandwidth Modified Super-Twisting Observer

Lianpeng Zhang, Cheng Liu *, Jingyuan Zhang and Rongchang Li

College of Electrical and Information Engineering, Beihua University, Jilin 132000, China; zhanglianpeng2024@163.com (L.Z.); zjy15134700244@163.com (J.Z.); lirongchang722@163.com (R.L.)
* Correspondence: liucheng@beihua.edu.cn

Abstract

In response to the severe chattering, slow dynamic response, and limited disturbance rejection capability of switched reluctance motor (SRM) drive systems under conventional control methods, this paper develops an improved nonsingular fast terminal sliding mode controller (INFTSMC). An integral sliding surface is first designed to eliminate the steady-state tracking error. An adaptive exponent and an improved double-power reaching law are then introduced to enhance the convergence performance. In addition, a smooth hyperbolic tangent approximation and a boundary layer design are employed instead of the conventional signum function to suppress chattering while maintaining a rapid response. Theoretical analysis demonstrates that the sliding variable is globally asymptotically stable and enters any prescribed neighborhood of the origin within a fixed time independent of the initial condition, thereby establishing practical fixed-time convergence rather than exact finite-time stability. Furthermore, an error-dependent bandwidth scheduling mechanism is incorporated into the modified super-twisting observer, resulting in an adaptive bandwidth modified super-twisting observer (AB-MSTO) for load torque estimation and compensation. The proposed bandwidth scheduling mechanism improves the balance between transient estimation speed and steady-state noise sensitivity. Finally, a MATLAB/Simulink simulation platform is constructed to evaluate the proposed control strategy. The simulation results demonstrate that the proposed INFTSMC combined with the AB-MSTO improves the dynamic speed regulation performance and disturbance rejection capability of the SRM drive system under different operating conditions.

Keywords: switched reluctance motor; nonsingular fast terminal sliding mode control; integral sliding surface; improved double-power law; adaptive bandwidth-modified super-twisting observer; load torque estimation

Check for updates

Academic Editor: Krzysztof Górecki

Received: 1 July 2026
Revised: 27 July 2026
Accepted: 29 July 2026
Published: 30 July 2026

Copyright: © 2026 by the authors. Licensee MDPI, Basel, Switzerland. This article is an open access article distributed under the terms and conditions of the Creative Commons Attribution (CC BY) license.

1. Introduction

In recent years, the rapid growth of new energy vehicles, electric aviation, and high-performance industrial servo systems has driven motor drives toward higher power density, efficiency, and reliability, thereby imposing more stringent requirements on both the motor and its control strategy. Owing to its simple structure, high mechanical robustness, high-temperature capability, rare-earth-free design, high starting torque, and wide speed

regulation range, the switched reluctance motor has attracted substantial attention in applications such as electric vehicles, rail transportation, and industrial drives [1]. In addition, in starter/generator systems, the SRM is widely regarded as a promising candidate for aviation electrification because of its inherent reliability and fault-tolerant capability [2]. Nevertheless, the doubly salient structure and strong magnetic nonlinearity of SRMs lead to pronounced electromagnetic torque ripple, significant acoustic noise, and challenges in accurate modeling [3–5]. These issues become more severe under wide speed and high-torque operation, where torque fluctuations can further evolve into speed oscillations and mechanical vibration, limiting SRM deployment in high-performance drives. Therefore, while preserving the structural simplicity and cost advantages of SRMs, improving speed smoothness and disturbance rejection while further suppressing torque ripple remains a key research challenge.

To address the above challenges, extensive efforts have been made worldwide from the perspectives of machine design, power conversion/drive, and control. From the control perspective, existing high-performance SRM speed regulation studies can be broadly classified into three technical directions. First, intelligent optimization and adaptive control: Ref. [6] develops an ANFIS-based control architecture optimized using the Border Collie Optimization algorithm for rotor position estimation and torque ripple minimization in an 8/6 SRM. Ref. [7] proposes a two-stage adaptive strategy for speed regulation and torque ripple optimization in electric vehicle applications, where particle swarm optimization is used offline to obtain initial parameters and extremum seeking is employed for online refinement, achieving improved speed tracking and torque smoothness over a wide operating range. However, such methods may involve complex optimization procedures and rely heavily on accurate system modeling and parameter tuning. Second, robust speed regulation based on active disturbance rejection control (ADRC): Ref. [8] develops an ADRC-based integrated control strategy for bearingless SRMs to improve the dynamic and steady-state performance of torque and suspension force control systems. Ref. [9] introduces an autoswitching upgraded ADRC scheme to balance transient response and steady-state accuracy under varying operating conditions; however, the performance of ADRC-based methods may be affected by observer bandwidth selection and controller gain tuning. Third, predictive, sliding-mode, and sensorless control methods: Ref. [10] presents a model predictive torque control approach with PWM generation based on linear polynomial fitting, in which phase torque and current prediction are incorporated to achieve fast dynamic response and torque ripple suppression. Ref. [11] proposes a super-twisting sliding mode observer based on a machine learning model for position sensorless control of SRM drives. Ref. [12] develops a super-twisting sliding mode control strategy for the speed and current loops of SRM drives, improving tracking performance and robustness under electric vehicle operating conditions. Ref. [13] proposes a direct instantaneous torque control strategy based on an improved sliding mode controller and disturbance observer to enhance torque regulation performance. Ref. [14] introduces a high-precision injection current sampling scheme for direct drive low-speed position sensorless control of switched reluctance machines. Overall, although these methods demonstrate strong adaptability and disturbance rejection capabilities under complex operating conditions, they may still suffer from increased computational complexity, dependence on model accuracy or data resources, chattering phenomena in sliding mode control, and trade-offs between rapid disturbance estimation and effective torque ripple suppression.

The super-twisting algorithm has been widely employed in second-order sliding mode controllers and observers because it can generate a continuous correction signal while maintaining strong robustness against matched disturbances. To improve its convergence characteristics, Moreno and Osorio developed the modified super-twisting algorithm

by incorporating additional linear feedback terms into the conventional super-twisting structure [15]. This modified structure combines the robustness of second-order sliding modes with the convergence characteristics of linear error feedback. Subsequently, modified and related super-twisting schemes have been applied to motor drive systems. For example, a modified super-twisting-based speed controller combined with an extended state observer was developed for SPMSM drives [16]. A super-twisting observer-based position sensorless drive with online parameter estimation was proposed for a magnetic suspension centrifugal compressor driven by a high-speed permanent magnet synchronous motor [17]. In addition, a modified super-twisting-based disturbance observer was employed in second-order sliding mode position control of permanent magnet synchronous motors [18]. Nevertheless, fixed-gain observer implementations generally involve a trade-off between rapid transient estimation and steady-state noise sensitivity. To address this issue, an error-dependent bandwidth scheduling mechanism is incorporated into the modified super-twisting observer in this study, resulting in an adaptive bandwidth modified super-twisting observer. The proposed AB-MSTO is integrated with the INFTSMC to estimate and compensate for the load torque in the switched reluctance motor drive.

Building on the above analysis, this paper proposes a high-performance SRM speed regulation strategy that combines an improved nonsingular fast terminal sliding mode control scheme with an adaptive-bandwidth modified super-twisting observer, without modifying the motor structure or power topology. Compared with conventional terminal sliding mode controllers, the proposed INFTSMC introduces an improved nonsingular fast terminal sliding surface, which accelerates error convergence while avoiding singularity problems and reducing steady-state tracking errors. Compared with existing sliding mode observers and super-twisting observers, the proposed AB-MSTO improves disturbance estimation accuracy and enhances robustness against parameter variations and external disturbances.

The proposed INFTSMC method employs hyperbolic tangent functions and piecewise continuous functions to replace the conventional sign function, resulting in a concise control law structure that involves only basic algebraic operations and saturation function calculations, facilitating digital processor implementation. To verify the effectiveness of the control strategy, simulation studies are conducted based on the MATLAB R2024b/Simulink platform, with four groups of typical operating condition experiments designed: high-speed starting with dynamic load, low-speed starting with dynamic load, high torque with dynamic speed, and low torque with dynamic speed.

The effectiveness of the proposed method is quantitatively verified through comprehensive internal benchmarking against conventional proportional–integral–derivative (PID) control and modern super-twisting sliding mode control (STSMC) under four typical operating conditions, with detailed motor-specific numerical results presented in Section 4, with comprehensive evaluation of each method's control performance in terms of speed response, torque ripple, current quality, and anti-load disturbance capability, providing theoretical basis and simulation verification for the engineering application of the proposed method.

2. Working Principle and Mathematical Model of SRM

Unlike conventional AC machines, which apply an alternating supply to the stator windings to establish a rotating magnetic field in the air gap, an SRM adopts a typical doubly salient structure: both the stator and rotor salient poles are formed by laminated silicon steel sheets without using permanent magnets, and the phase windings are concentrated on the stator teeth; its electromechanical energy conversion follows the principle that magnetic flux always closes along the path of minimum reluctance [19–21]. Figure 1

illustrates the structure of a typical 12/8-pole switched reluctance motor, which consists of 12 stator poles and 8 rotor poles.

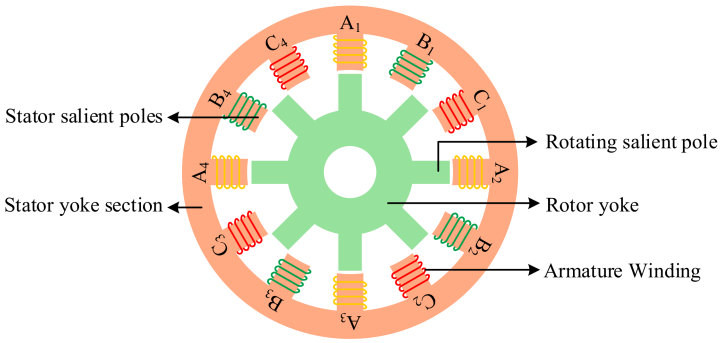


Figure 1. Structure of a typical 12/8-pole switched reluctance motor.

The instantaneous electromagnetic torque generated by the k-th phase can be expressed in terms of the magnetic co-energy or magnetic field energy as

$$T_k(i_k,\theta) = \left.\frac{\partial W'_k(i_k,\theta)}{\partial\theta}\right|_{i_k=\text{const}} = -\left.\frac{\partial W_k(\psi_k,\theta)}{\partial\theta}\right|_{\psi_k=\text{const}}. \quad (1)$$

The magnetic co-energy of the k-th phase is defined as

$$W'_k(i_k,\theta) = \int_0^{i_k} \psi_k(\iota,\theta)\mathrm{d}\iota. \quad (2)$$

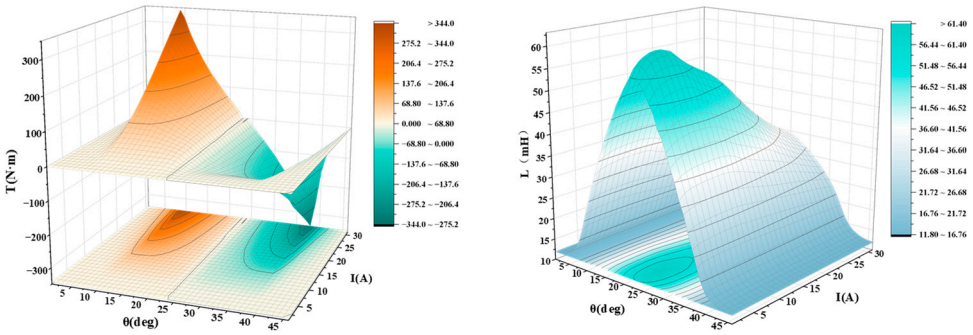
The total electromagnetic torque of the motor is obtained by summing the torque contributions of all phases:

$$T_e = \sum_{k=1}^{m} T_k(i_k,\theta). \quad (3)$$

where T_e denotes the total electromagnetic torque generated by the motor, k denotes the phase index, m is the number of motor phases, i_k is the instantaneous phase current, ψ_k is the phase flux linkage, θ is the rotor position, $W_k'(i_k,\theta)$ is the magnetic co-energy, $W_k(\psi_k,\theta)$ is the magnetic field energy, and ι is the integration variable.

In the simulation model, the nonlinear electromagnetic characteristics of the SRM were obtained through offline two-dimensional finite element analysis over the prescribed ranges of phase current and rotor position. The resulting phase flux-linkage data $\psi_k(i_k,\theta)$ and static electromagnetic torque data $T_k(i_k,\theta)$ were stored as two-dimensional lookup tables in MATLAB/Simulink. During simulation, the instantaneous phase flux linkage and electromagnetic torque were evaluated by two-dimensional interpolation according to the phase current and rotor position. Consequently, magnetic saturation, rotor-position-dependent inductance, and nonlinear torque production were retained in the SRM model instead of using a constant-inductance approximation. The same nonlinear electromagnetic characteristic maps were used for all comparative simulations.

Due to the strong magnetic nonlinearity and complex flux distribution in an SRM, it is difficult to establish an accurate analytical relationship among flux linkage, inductance, torque, phase current, and rotor position angle. To obtain a high-fidelity model, this paper employs finite element analysis (FEA) to extract key electromagnetic characteristics and constructs three-dimensional nonlinear inductance and torque characteristic surfaces (see Figure 2). Considering the real-time requirements of torque control, the extracted data are incorporated into the simulation model in the form of look-up tables, enabling rapid acquisition of instantaneous torque at different rotor position angles.



(**a**) (**b**)

Figure 2. Characteristic curves: (**a**) torque characteristics; (**b**) inductance characteristics.

To obtain a high-fidelity SRM model, the nonlinear magnetic characteristics of the SRM shown in Figure 2 were obtained through finite element analysis using 600W50 silicon steel as the stator and rotor core material. Considering the periodicity of the SRM magnetic characteristics, the rotor position was normalized within one electrical period (0–45°) through a modulo operation. The flux linkage and torque characteristics were generated with current sampling intervals of 1 A over a current range of 0–30 A and rotor-position sampling intervals of 1° within the range of 0–45°. The obtained nonlinear magnetic data were stored in lookup tables and implemented in the MATLAB/Simulink model. During the simulation, the lookup tables were used to obtain the corresponding flux linkage and torque values according to the instantaneous phase current and rotor position. In the DITC strategy, the turn-on and turn-off angles were set to 5° and 20°, respectively.

3. Design of an Improved Nonsingular Fast Terminal Sliding Mode Controller

To improve the dynamic performance and robustness of the outer speed loop, this paper introduces an improved nonsingular fast terminal sliding mode controller into the conventional outer loop scheme and optimizes both the sliding surface and the reaching law. The resulting controller achieves fast convergence, low chattering, and strong disturbance rejection, making it suitable for high-performance SRM speed regulation over a wide operating range.

3.1. Design of an Improved Nonsingular Fast Terminal Integral Sliding Surface

According to the control requirements, this paper proposes a novel nonsingular fast terminal sliding mode controller. An improved integral sliding surface with an adaptive power term is adopted to avoid singularity and accelerate convergence in the small error region, while the integral term is used to suppress steady-state bias and low-frequency disturbances and to reduce the reliance on high switching gains. The improved integral sliding surface is defined as follows:

$$s = E_\omega + a_1 \int_0^t E_\omega \, dt + a_2 \int_0^t |E_\omega|^{\lambda(E_\omega)} \mathrm{sgn}(E_\omega) dt \tag{4}$$

$$\lambda(E_\omega) = \lambda_0 + \lambda_1 \exp\left(-\frac{|E_\omega|}{e_0}\right) \tag{5}$$

where E_ω denotes the speed tracking error, a_1 and a_2 are positive design parameters, e_0 is a positive scaling factor, and λ_0 and λ_1 are adaptive coefficients. The function $\lambda(E_\omega)$ is introduced to provide fractional power behavior near the origin and improve the convergence performance of the nonlinear integral channel, which enables the nonlinear integral channel to exhibit "fractional-power" behavior in the near-origin region. This is consistent with the

terminal power term in the reaching law, thereby avoiding singularity while simultaneously improving the recovery speed under small errors. The linear integral part eliminates steady-state error and suppresses low-frequency disturbances by integrating persistent errors into an additional driving force, which pushes the trajectory to approach s = 0 more rapidly and, while maintaining convergence speed, significantly reduces the reliance on large switching gains and the associated chattering risk. The nonlinear integral part offers a pronounced advantage in accelerating the approach to the origin in the near region while avoiding the singularity inherent in conventional terminal sliding mode designs.

The "nonsingular" attribute of the proposed sliding surface lies in avoiding the unbounded control input problem that occurs in conventional terminal sliding mode control when the system state approaches the equilibrium. Conventional terminal sliding mode employs a fixed fractional power $\lambda << 1$, where the term $|E_\omega|^{\lambda-1} \to \infty$ as $E_\omega \to 0$ in the derivative of the sliding surface, leading to infinite control input, actuator saturation, and even system instability.

This paper adopts an adaptive power $\lambda(E_\omega) = \lambda$ combined with an integral form sliding surface to fundamentally eliminate singularity: when far from equilibrium ($|E_\omega| >> e_0$), $\lambda \to \lambda_0 + \lambda_1$, and the surface degenerates to an approximately linear form, avoiding the amplification effect of fractional power; when near equilibrium ($|E_\omega| \to 0$), $\lambda \to \lambda_0$, and although fractional, the derivative of the integral term $\int |E_\omega| \lambda \mathrm{sgn}(E_\omega) d\tau$ yields $|E_\omega|^\lambda$, which approaches 0 rather than infinity, ensuring bounded control input. Mathematically, the control input $u = -\varepsilon \mathrm{sgn}(s) - ks$ remains bounded since s is always finite.

Compared with the linear sliding surface $s = E_\omega + c\int E_\omega d\tau$, the proposed surface maintains nonsingularity (control input always bounded) while achieving finite-time convergence through the adaptive fractional power, overcoming the slow asymptotic convergence drawback of linear sliding mode.

Figure 3 Comparison of speed error convergence between the conventional sliding surface and the proposed novel sliding surface in a switched reluctance motor drive system, using the same reaching law:

$$\dot{s} = -k_T \tanh\left(\frac{s}{\phi}\right) \tag{6}$$

where s represents the sliding surface, k_T is the switching gain, and ϕ is the boundary layer thickness parameter used to smooth the switching function and reduce chattering. The mechanical dynamic equation of the SRM is given by the following expression:

$$J\frac{d\omega}{dt} = T_e - T_L - B\omega \tag{7}$$

with J = 0.0015 kg·m^2, B = 0.002 N·m·s/rad, and no load ($T_L = 0$). Initial speed $\omega(0) = 0$; reference speed $\omega_{ref} = 100$ rad/s. The conventional sliding surface ($c_0 = 2$, where c_0 denotes the integral gain of the conventional sliding surface) is

$$s = E_\omega + c_0 \int E_\omega dt \tag{8}$$

To evaluate the convergence performance of the proposed sliding surface, a comparative simulation is conducted between the proposed surface and the traditional sliding surface under identical conditions. The initial speed error, reference condition, and reaching law parameters are kept the same for both methods. The parameters of the proposed surface are set as p = 8, q = 30, $\lambda_0 = 0.3$, $\lambda_1 = 0.7$, $E_{\omega 0}$ =2.0. For a fair comparison, both the proposed and traditional surfaces employ the same reaching law parameters, with $\varepsilon = 5$, $\phi = 0.5$. As illustrated in Figure 3, the proposed surface enables the speed error to converge within the range of ± 0.5 rad/s in approximately 0.35 s, whereas the traditional surface

requires a longer convergence time. This result demonstrates that, under identical reaching law conditions, the proposed surface provides improved convergence performance.

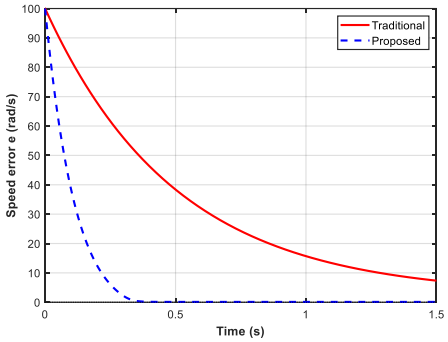


Figure 3. Comparison of the two sliding surfaces.

As shown in Figure 3, a comparison between the nonsingular terminal sliding surface and the conventional linear sliding surface indicates that the former requires less time and achieves a faster reaching speed as the state trajectory approaches the sliding manifold s = 0. Therefore, compared with the traditional sliding surface, it exhibits a significantly higher convergence rate.

3.2. Design of an Improved Double-Power Convergence Law

The conventional nonsingular fast terminal sliding mode (NFTS) reaching law has been widely investigated because of its rapid convergence characteristics and is generally expressed [22] as

$$\dot{s} = -k_1|s|^{\alpha}\mathrm{sgn}(s) - k_2|s|^{\beta}\mathrm{sgn}(s) \tag{9}$$

where k_1 and k_2 are positive reaching gains, α and β are power exponents satisfying $k_1 > 0$, $k_2 > 0$, $\alpha > 1$, and $0 < \beta < 1$. The high-order power term provides a strong driving action when the system state is far from the sliding manifold, whereas the fractional power term accelerates the convergence process near the origin. However, the discontinuous sign function may cause severe chattering, thereby limiting the application of the conventional reaching law in high-precision switched reluctance motor speed regulation systems.

To alleviate chattering while maintaining a rapid reaching process, an improved double-power reaching law is proposed. A narrow-band interpolation function is introduced to provide a continuous transition between the fractional power term in the near region and the quadratic power term in the far region. Moreover, smooth hyperbolic tangent functions and a boundary layer damping term are employed instead of the discontinuous sign function. The proposed reaching law is expressed as

$$\dot{s} = -k_1|s|^{p/q}\tanh(s) - k_2H(s)\tanh(s) - c\left[\tanh\left(\frac{s}{\Delta}\right) + s\right] \tag{10}$$

where k_1, k_2, and c are positive control gains; p and q are positive integers satisfying $0 < p < q$, such that $0 < p/q < 1$; $\Delta > 0$ denotes the boundary layer thickness of the hyperbolic tangent function; and $H(s)$ is a continuous interpolation function used to smoothly connect the different power terms. To avoid abrupt switching between different power terms, a continuous transition function is introduced. The function is constructed by smoothly blending the fractional power term and quadratic term in different error regions, which improves the continuity of the proposed convergence law. The interpolation function *H(s)* is defined as

$$H(s) = \begin{cases} |s|^{p/q}, & 0 \le |s| \le 1-\delta \\ a(s)|s|^2 + [1-a(s)]|s|^{p/q}, & 1-\delta < |s| < 1+\delta \\ |s|^2, & |s| \ge 1+\delta \end{cases} \tag{11}$$

where

$$\alpha(s) = \frac{|s| - (1-\delta)}{2\delta} \tag{12}$$

where δ defines the transition boundary, and α(s) is a continuous weighting function used to ensure a smooth transition between the two power terms. The construction of this function follows the continuous nonlinear switching strategy reported in [23].

The design parameters satisfy $0 < p/q < 1$, $0 < \delta < 1$, $\Delta > 0$, $k_1 > 0$, $k_2 > 0$, $c > 0$, and $T_f > 0$. Here, δ determines the half-width of the interpolation interval, whereas Δ denotes the thickness of the hyperbolic tangent boundary layer.

The continuity of H(s) can be verified at the two junction points. At $|s| = 1-\delta$, $a(s) = 0$, and the middle branch of (9) reduces to $H(s) = |s|^{p/q}$; therefore, the left- and right-hand values of H(s) are both equal to $(1-\delta)^{p/q}$. At $|s| = 1+\delta$, $a(s) = 1$, and the middle branch reduces to $H(s) = |s|^2$; hence, the left- and right-hand values are both equal to $(1+\delta)^2$. Thus, H(s) is continuous over its entire domain. Since all the remaining terms in (8) are also continuous, the proposed reaching law avoids numerical jumps at the switching boundaries. The linear interpolation provides a smooth transition between different convergence regions and improves numerical stability during implementation.

The gains of the proposed reaching law are selected as

$$k_1 = \frac{4}{T_f}, \quad k_2 = \frac{4}{T_f}, \quad c = \frac{2}{T_f}. \tag{13}$$

In this study, $T_f = 0.024$ s is adopted, yielding $k_1 = k_2 = 166.67$ and $c = 83.33$. These values are identical to those implemented in the simulation model. Because smooth hyperbolic tangent functions are employed in (8), T_f is treated as a gain scaling parameter rather than an unconditional exact settling time to the origin. Its relationship with the practical convergence time bound is established below.

When $|s| \ge 1+\delta$, the quadratic term $H(s) = |s|^2$ provides a strong driving action and rapidly reduces large sliding errors. When $|s| \le 1-\delta$, the fractional power term improves the convergence performance for small errors. The hyperbolic tangent terms provide smooth control action near the origin and alleviate chattering. Therefore, the proposed reaching law combines rapid far-region attraction with smooth near-origin behavior.

To analyze stability, consider the Lyapunov function

$$V = \frac{1}{2}s^2 \tag{14}$$

Taking the time derivative of V along the trajectories of (8) gives

$$\begin{aligned} \dot{V} &= s\dot{s} \\ &= -k_1|s|^{p/q+1}\tanh(|s|) - k_2|s|H(s)\tanh(|s|) \\ &\quad -c|s|\tanh\left(\tfrac{|s|}{\Delta}\right) - cs^2. \end{aligned} \tag{15}$$

For every $s \neq 0$, $\tanh(|s|) > 0$, $H(s) > 0$, and $\tanh(|s|/\Delta) > 0$; therefore, $\dot{V} < 0$. Since V is positive definite and radially unbounded and $\dot{V}$ is negative definite, the equilibrium $s = 0$ is globally asymptotically stable. Moreover, $V(t) \le V(0)$ for all $t \ge 0$, and hence s(t) remains bounded.

Because the hyperbolic tangent functions make the vector field locally Lipschitz in a neighborhood of the origin, the proposed smooth reaching law guarantees asymptotic convergence to s = 0, rather than exact finite time arrival at the origin. Nevertheless, it guarantees that s enters any prescribed neighborhood $|s| \leq \varepsilon$, where $0 < \varepsilon < 1 - \delta$, within a time bound that is independent of the initial condition. Here, ε is an analysis tolerance used to characterize practical convergence and is not an additional controller parameter.

Let $x = |s|$. For $s \neq 0$, the dynamics of x are Let $x = |s|$. For $s \neq 0$, the derivative of x can be expressed as $\dot{x} = sgn(s)\dot{s}$. Substituting (8) into this expression yields the following dynamics of x:

$$\dot{x} = -k_1 x^{p/q}\tanh(x) - k_2 H(x)\tanh(x) - c\tanh\left(\frac{x}{\Delta}\right) - cx \tag{16}$$

When $x \geq 1 + \delta$, $H(x) = x^2$ and $\tanh(x) \geq \tanh(1 + \delta)$. By retaining only the quadratic reaching term, one obtains

$$\dot{x} \leq -k_2\tanh(1 + \delta)x^2 \tag{17}$$

Integrating (15), the time required for x to enter the region $x \leq 1 + \delta$ from any finite initial condition satisfies

$$T_1 \leq \frac{1}{k_2(1 + \delta)\tanh(1 + \delta)} \tag{18}$$

For $\varepsilon \leq x \leq 1 + \delta$, the monotonicity of the hyperbolic tangent function gives $\tanh(x/\Delta) \geq \tanh(\varepsilon/\Delta)$. Consequently,

$$\dot{x} \leq -c\tanh\left(\frac{\varepsilon}{\Delta}\right) \tag{19}$$

The time required for x to move from $1 + \delta$ to the prescribed neighborhood $x \leq \varepsilon$ therefore satisfies

$$T_2 \leq \frac{1 + \delta - \varepsilon}{c\tanh(\varepsilon/\Delta)} \tag{20}$$

Combining (18) and (20), the total practical convergence time satisfies

$$\begin{aligned} T_\varepsilon &\leq T_1 + T_2 \\ &\leq \frac{1}{k_2(1+\delta)\tanh(1+\delta)} + \frac{1+\delta-\varepsilon}{c\tanh(\varepsilon/\Delta)} \end{aligned} \tag{21}$$

The upper bound in (21) is independent of the initial value $s(0)$. Hence, the proposed reaching law guarantees practical fixed-time convergence to the prescribed neighborhood $|s| \leq \varepsilon$.

Substituting the gain selection expressions in (11) into (19) yields

$$T_\varepsilon \leq T_f\left[\frac{1}{4(1 + \delta)\tanh(1 + \delta)} + \frac{1 + \delta - \varepsilon}{2\tanh(\varepsilon/\Delta)}\right] \tag{22}$$

Define $C_\varepsilon = 1/[4(1 + \delta)\tanh(1 + \delta)] + (1 + \delta - \varepsilon)/[2\tanh(\varepsilon/\Delta)]$. Then, $T_\varepsilon \leq C_\varepsilon T_f$. For $T_f = 0.024$ s, the practical convergence time bound becomes $T_\varepsilon \leq 0.024 C_\varepsilon$ s.

If a prescribed practical convergence time $T_d > 0$ is required, the gain scaling parameter can be selected to satisfy

$$T_f \leq \frac{T_d}{C_\varepsilon} \tag{23}$$

which guarantees $T_\varepsilon \leq T_d$. Equations (22) and (23) explicitly establish how the gain selection in (13) determines the practical convergence time bound. A smaller T_f produces larger k_1, k_2, and c, thereby reducing the theoretical convergence time upper bound. After the sliding variable enters the neighborhood $|s| \leq \varepsilon$, the negative definite Lyapunov derivative in (15) guarantees asymptotic convergence to the origin.

For the closed-loop boundedness analysis, it is assumed that the reference speed and its required derivatives are bounded, the lumped disturbance and its estimation error are bounded, and the input coefficient of the SRM speed dynamics is continuous and satisfies $0 < b_{min} \leq b(x) \leq b_{max}$. Since $V(t) \leq V(0)$, the sliding variable s is bounded. For bounded s, all terms in the reaching law (8) are continuous and bounded. Furthermore, the proposed sliding surface contains no negative powers of the tracking error and therefore does not introduce a singularity. Under the bounded input bounded state property of the tracking error dynamics established in Section 3.1, the boundedness of s implies that the speed tracking error and the auxiliary integral state remain bounded. Since $b(x)$ is bounded away from zero and the reference, model, disturbance compensation, and reaching law terms are bounded, the control input also remains bounded. Therefore, all controller-side closed-loop signals remain bounded for finite initial conditions.

Therefore, the proposed smooth double-power reaching law guarantees global asymptotic convergence of the sliding variable to the origin and practical fixed-time convergence to any prescribed neighborhood $|s| \leq \varepsilon$. Because the hyperbolic tangent terms render the closed-loop vector field locally Lipschitz near the origin, exact finite-time convergence to s = 0 is not guaranteed. Hence, the established property is global asymptotic stability of the sliding variable together with practical fixed-time convergence to a prescribed neighborhood, rather than exact finite-time stability of the origin.

In summary, the proposed improved double-power reaching law guarantees global asymptotic stability of the sliding variable, practical fixed-time convergence to an arbitrarily prescribed neighborhood, continuity at the switching boundaries, and boundedness of the controller-side closed-loop signals. Compared with the conventional NFTS reaching law, the proposed method achieves a better compromise among convergence speed, chattering suppression, and numerical smoothness.

Figure 4 Comparison of INFTSMC and NFTSMC reaching laws in the SRM speed control system. The simulation employs the SRM mechanical model with parameters J = 0.0015 kg·m^2, D = 0.002 N·m·s/rad, and a linear integral sliding surface $s = e + c\int e dt$ (c = 5). The initial condition is s(0) = 2.0. As shown in Figure 4a, INFTSMC exhibits a larger reaching speed when far from the sliding surface ($|s| > 1$), benefiting from the $|s|^2$ term in H(s). The log-scale plot in Figure 4b reveals that $|ds/dt|$ of INFTSMC decays smoothly to negligible values as $s \to 0$, while NFTSMC retains a residual reaching speed of approximately 0.097, demonstrating the superior chattering elimination of INFTSMC. Figure 4c presents the time response of s(t): INFTSMC (blue dashed) converges to zero within about 0.25 s, which is significantly faster than NFTSMC (red solid, about 0.8 s). Moreover, INFTSMC shows a smooth, oscillation-free transient, whereas NFTSMC exhibits noticeable chattering before convergence. The phase trajectory in Figure 4d further verifies the "soft landing" characteristic of INFTSMC—the curve approaches the origin smoothly without abrupt changes in $|ds/dt|$. In summary, INFTSMC achieves a balance between fast reaching and chattering-free performance through piecewise enhancement and continuous design, making it more suitable for precision control applications.

The mechanical dynamic equation of the SRM is shown in Equation (5).

By combining the above sliding surface and reaching law, the expression for the SRM electromagnetic torque is obtained as shown below.

$$T_{ref} = T_{eq} + T_{sw} \tag{24}$$

$$T_{eq} = T_L + B\omega + J\left(\dot{\omega}_{ref} + a_1 E_\omega + a_2 |E_\omega|^{\lambda(E_\omega)} sgn(E_\omega)\right) \tag{25}$$

$$T_{sw} = J\left(k_1|s|^{\frac{p}{q}}\tanh(s) + k_2 H(s)\tanh(s) + c\left(\tanh\left(\frac{s}{\Delta}\right) + s\right)\right) \tag{26}$$

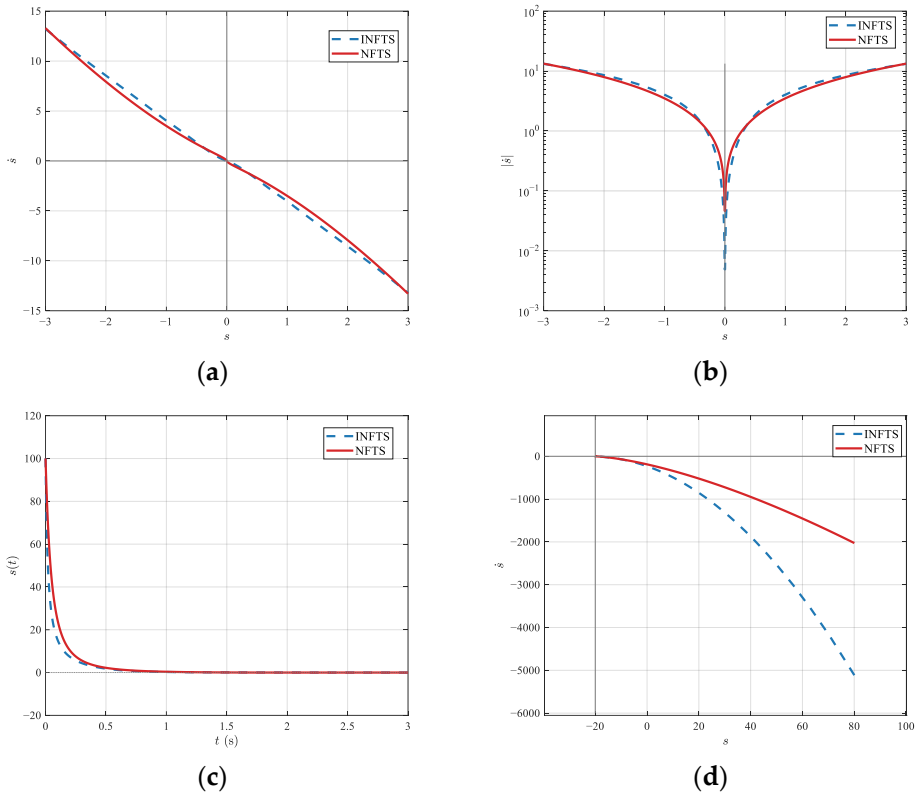


Figure 4. Comparison of INFTSMC and NFTSMC reaching laws in terms of (**a**) reaching law curves; (**b**) reaching speed; (**c**) sliding variable time response; (**d**) phase trajectory.

The control law (24)–(26) consists of two components: the equivalent control T_{eq} given by (25) and the switching control T_{sw} given by (26). In (25), T_L represents the load torque, $B\omega$ is the viscous damping term, and the bracketed terms correspond to the reference acceleration feedforward, linear error feedback, and nonlinear terminal attractor, respectively, which collectively maintain the ideal sliding motion. In (26), the switching control drives the system state toward the sliding surface with fast reaching and chattering suppression, where $k_1|\mathrm{s}|^{\mathrm{p/q}}$ provides the fractional power fast reaching term, $k_2H(s)$ enhances the reaching speed when far from the surface through the piecewise function, and c(tanh(s/Δ) + s) introduces the boundary layer smoothing and linear damping. The total electromagnetic torque reference T_{ref} is obtained by summing (25) and (26), ensuring both finite-time convergence and bounded control input. The block diagram of the improved nonsingular fast terminal sliding mode controller is presented in the following figure.

The nominal moment of inertia and viscous friction coefficient are obtained from the rated SRM parameters. The load torque is not assumed to be measurable or known in advance; instead, it is estimated online by the proposed AB-MSTO and used for feedforward compensation. Variations in the mechanical parameters and unmodeled dynamics are regarded as lumped uncertainties, whose effects are compensated by the observer estimate and the robust term of the sliding mode controller. The block diagram of the improved nonsingular fast terminal sliding mode controller is presented in Figure 5.

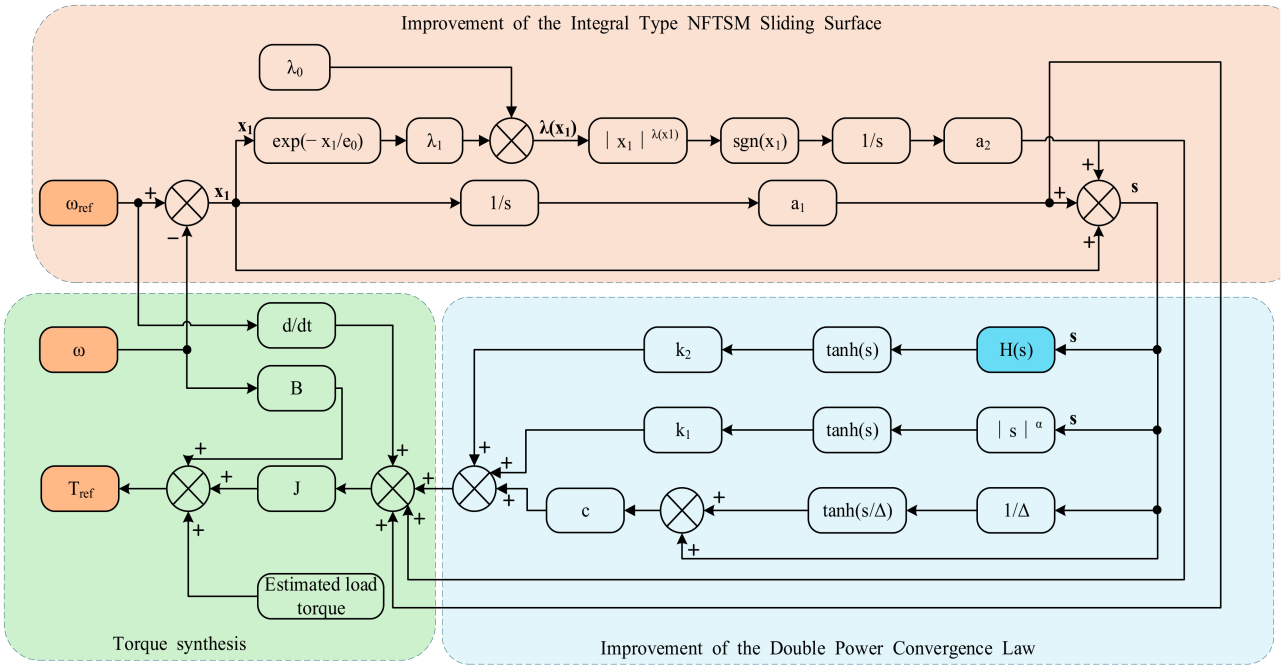


Figure 5. Block diagram of the improved nonsingular fast terminal sliding mode controller.

4. Adaptive Bandwidth Modified Super-Twisting Observer

To mitigate the influence of external load disturbances on system performance, this paper develops an adaptive bandwidth modified super-twisting observer to estimate the load torque online. The estimated load torque is introduced into the speed loop as a feedforward compensation term to improve the dynamic response and disturbance rejection capability of the switched reluctance motor drive system.

The mechanical system is augmented into a two-dimensional extended state model, in which $x_1 = \omega$ denotes the rotor speed and $x_2 = T_L$ denotes the load torque. The extended state equations are

$$\begin{cases} \dot{x}_1 = \omega = \frac{T_{ctrl} - T_L - B\omega}{J} \\ \dot{x}_2 = \dot{T}_L \end{cases} \tag{27}$$

where T_{ctrl} denotes the actual torque command applied to the SRM after the torque saturation process, while T_{ref} represents the reference electromagnetic torque generated by the speed controller. In the above model, the load torque T_L is assumed to be bounded and piecewise differentiable. Its derivative satisfies $\left|\dot{T}_L(t)\right| \le D_T$ almost everywhere, where $D_T > 0$ is a known upper bound. A finite number of bounded jump discontinuities is also permitted. This unified assumption includes constant and slowly varying loads as special cases, permits time-varying disturbances with bounded rates, and is consistent with the step load tests used in the simulation. At a load torque jump, the estimation error may change instantaneously but remains bounded, after which the observer reconverges on the subsequent continuous interval.

For the extended system, the observer estimates both the rotor speed and the load torque. The speed estimation error is defined as

$$e_\omega = \omega - \hat{\omega} \tag{28}$$

For the subsequent analysis, the load torque estimation error is additionally defined as $\widetilde{T}_L = T_L - \hat{T}_L$.

First, a linear extended state observer (LESO) is employed to estimate the speed and load torque. Its standard form is

$$\begin{cases} \dot{\hat{\omega}} = \frac{T_{ctrl} - \hat{T}_L - B\hat{\omega}}{J} + l_1 e_\omega \\ \dot{\hat{T}}_L = -l_2 e_\omega \end{cases} \tag{29}$$

The LESO has a simple structure and satisfactory far-region behavior. However, when the estimation error approaches zero, purely linear correction may result in a relatively slow convergence rate. To improve the near-origin convergence performance, a super-twisting sliding mode algorithm-based correction mechanism is connected in parallel with the linear LESO correction. By further introducing an adaptive bandwidth adjustment strategy, an adaptive bandwidth modified super-twisting observer is obtained. The proposed AB-MSTO is

$$\begin{cases} \dot{\hat{\omega}} = \frac{T_{ctrl} - \hat{T}_L - B\hat{\omega}}{J} + g_1 |e_\omega|^{1/2} \mathrm{sgn}(e_\omega) + l_1 e_\omega \\ \dot{\hat{T}}_L = -g_2 \mathrm{sgn}(e_\omega) - l_2 e_\omega \end{cases} \tag{30}$$

The nonlinear correction terms are functions of the estimation error e_ω rather than the rotor speed ω. This correction resolves the notation inconsistency in the previous version and ensures that the observer injection vanishes with the estimation error.

To facilitate tuning, the observer gains are generated using two physically interpretable parameters:

$$l_1 = 2\omega_0,\ l_2 = J\omega_0^2,\ g_1 = \xi\sqrt{\omega_0},\ g_2 = \xi J\omega_0^{3/2} \tag{31}$$

where g_1 and g_2 are the nonlinear super-twisting correction gains, and l_1 and l_2 are the linear observer gains. Here, ω_0 is the observer bandwidth, which determines the observer response speed, and $\xi > 0$ is the super-twisting strength coefficient, which regulates the convergence rate of the nonlinear correction mechanism. The symbol ξ is used consistently throughout this section. Increasing ξ accelerates convergence but may also increase sensitivity to measurement noise.

A fixed large observer bandwidth may amplify measurement noise, whereas a fixed small bandwidth may degrade dynamic performance. Therefore, a speed-estimation-error-based adaptive bandwidth strategy is adopted. The adaptive bandwidth is

$$\omega_0(e_\omega) = \omega_{near} + (\omega_{far} - \omega_{near}) S(|e_\omega|, e_{th}) \tag{32}$$

where the switching function is

$$S(|e_\omega|, e_{th}) = \frac{1}{1 + \exp[-k_s(|e_\omega| - e_{th})]} \tag{33}$$

where $S(|\ e_\omega\ |, e_{th})$ denotes a smooth switching function, e_ω is the speed estimation error, $e_{th} > 0$ is the prescribed error threshold, and $k_s > 0$ is the switching slope coefficient that determines the transition steepness between the near-origin and far-region bandwidths The adaptive bandwidth parameters satisfy $0 < \omega_{near} \leq \omega_{far}$, $k_s > 0$, and $e_{th} > 0$. Consequently, $\omega_0(e_\omega) \in [\omega_{near}, \omega_{far}]$, and all observer gains remain positive and bounded. For a large estimation error, the bandwidth approaches ω_{far} to accelerate the transient response. Near the origin, it approaches ω_{near} to reduce noise amplification.

Using the SRM mechanical equation and the AB-MSTO structure, the estimation error dynamics are obtained as follows:

$$\begin{cases} \dot{e}_\omega = -\left(\frac{B}{J} + l_1\right) e_\omega - k_1 |e_\omega|^{1/2} \mathrm{sgn}(e_\omega) - \frac{\tilde{T}_L}{J} \\ \dot{\tilde{T}}_L = \dot{T}_L + k_2 \mathrm{sgn}(e_\omega) + l_2 e_\omega \end{cases} \tag{34}$$

Define $\nu = -\tilde{T}_L/J$ and $d(t) = -\dot{T}_L/J$. Then $|d(t)| \leq D$, where $D = D_T/J$.

The following finite-time convergence analysis is developed based on the strong Lyapunov framework for the modified super-twisting algorithm established in [15]. The transformed estimation error dynamics preserve the modified super-twisting structure, while the adaptive bandwidth generates bounded state-dependent gains.

The error system can consequently be rewritten as

$$\begin{cases} \dot{e}_\omega = -ae_\omega - \lambda_0 |e_\omega|^{1/2} \mathrm{sgn}(e_\omega) + \nu \\ \dot{\nu} = -\alpha_0 \mathrm{sgn}(e_\omega) - \beta_0 e_\omega + d(t) \end{cases} \tag{35}$$

The coefficients in the transformed error system are defined as

$$a = \frac{B}{J} + l_1, \;\; \lambda_0 = g_1, \;\; \alpha_0 = \frac{g_2}{J}, \;\; \beta_0 = \frac{l_2}{J} \tag{36}$$

Because the adaptive bandwidth is bounded, the fractional power gain satisfies

$$\lambda_{0\min} = \xi\sqrt{\omega_{near}}, \;\; \lambda_{0\max} = \xi\sqrt{\omega_{far}}, \;\; \lambda_{0\min} \le \lambda_0(e_\omega) \le \lambda_{0\max} \tag{37}$$

and the integral sign-related gain satisfies

$$\alpha_{0\min} = \xi\omega_{near}^{3/2}, \;\; \alpha_{0\max} = \xi\omega_{far}^{3/2}, \;\; \alpha_{0\min} \le \alpha_0(e_\omega) \le \alpha_{0\max} \tag{38}$$

A sufficient disturbance dominance condition is $\alpha_0 \mathrm{min} > \mathrm{D}$. To provide a formal and directly checkable finite-time condition, define

$$z_1 = |e_\omega|^{1/2} \mathrm{sgn}(e_\omega), \;\; z_2 = \nu, \;\; z = [z_1 \; z_2]^T \tag{39}$$

For $\mathrm{e}_\omega \neq 0$, the super-twisting core of the transformed error dynamics can be represented by the uncertain matrix

$$A(\lambda_0, \alpha_0, \mu) = \begin{bmatrix} -\lambda_0/2 & 1/2 \\ -(\alpha_0 - \mu) & 0 \end{bmatrix}, \;\; |\mu| \le D \tag{40}$$

Following the strong Lyapunov framework established for the modified super-twisting algorithm, a sufficient condition for uniform finite-time convergence over the admissible adaptive gain and disturbance ranges is the existence of common symmetric matrices $\mathrm{P} = \mathrm{P}^{\mathrm{T}} > 0$ and $\mathrm{Q} = \mathrm{Q}^{\mathrm{T}} > 0$ satisfying

$$A^T(\lambda_0, \alpha_0, \mu)P + PA(\lambda_0, \alpha_0, \mu) \le -Q \tag{41}$$

Because the matrix inequality is affine with respect to λ_0, α_0, and μ, it is sufficient to impose the condition at the following vertices:

$$\lambda \in \{\lambda_{0\min}, \lambda_{0\max}\}, \; \alpha \in \{\alpha_{0\min}, \alpha_{0\max}\}, \; \mu \in \{-D, D\} \tag{42}$$

Since the matrix inequality is affine in λ_0, α_0, and μ, satisfaction at all vertices is sufficient for satisfaction over the complete admissible parameter ranges. Under this common Lyapunov sufficient condition, define

$$V_o = z^T P z \tag{43}$$

The derivative of the Lyapunov function satisfies

$$\dot{V}_o \le -c_o V_o^{1/2}, \;\; c_o > 0 \tag{44}$$

Integrating the above inequality yields the following upper bound on the settling time:

$$T_o - t_0 \leq \frac{2\sqrt{V_o(t_0)}}{c_o}, \tag{45}$$

where t_0 denotes the initial time of the considered continuous interval of the load torque disturbance. Therefore, under the stated disturbance dominance and common Lyapunov sufficient conditions, the speed estimation error and load torque estimation error converge to zero in finite time during each continuous interval in which the load torque is differentiable.

The additional linear correction terms $-\alpha_0 e_\omega$ and $-\beta_0 e_\omega$ are part of the modified super-twisting structure considered. These terms are continuous and vanish at the origin. Under the sufficient conditions stated above, they do not invalidate the finite-time convergence property of the modified super-twisting error dynamics.

At a bounded load torque jump, T_L remains bounded, although the load torque estimation error may change instantaneously. After the jump, the same finite-time convergence argument applies on the subsequent continuous interval, provided that the disturbance dominance and common Lyapunov sufficient conditions remain satisfied. Thus, the adaptive bandwidth is restricted to an admissible bounded range and does not change the implemented observer structure.

The structure diagram of the proposed adaptive bandwidth modified super-twisting observer is shown in Figure 6.

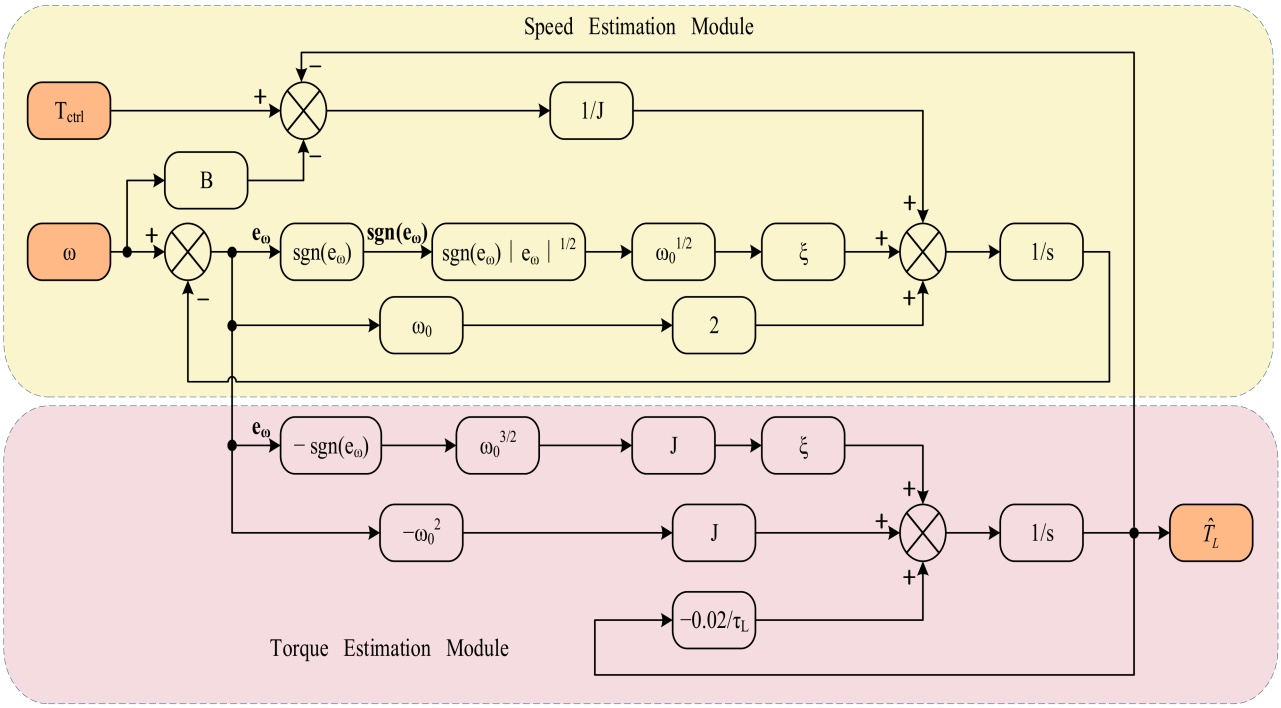


Figure 6. Structural diagram of the adaptive bandwidth modified super-twisting observer.

To evaluate the dynamic load torque estimation performance of the proposed AB-MSTO in the SRM drive system, a conventional linear extended state observer (LESO), which is commonly used for lumped disturbance and load torque estimation in motor drives, is selected as the benchmark observer. Step load changes are applied under two representative operating conditions, namely high-speed startup and low-speed operation. The load torque estimation results and estimation errors obtained using the AB-MSTO and LESO are compared in Figure 7.

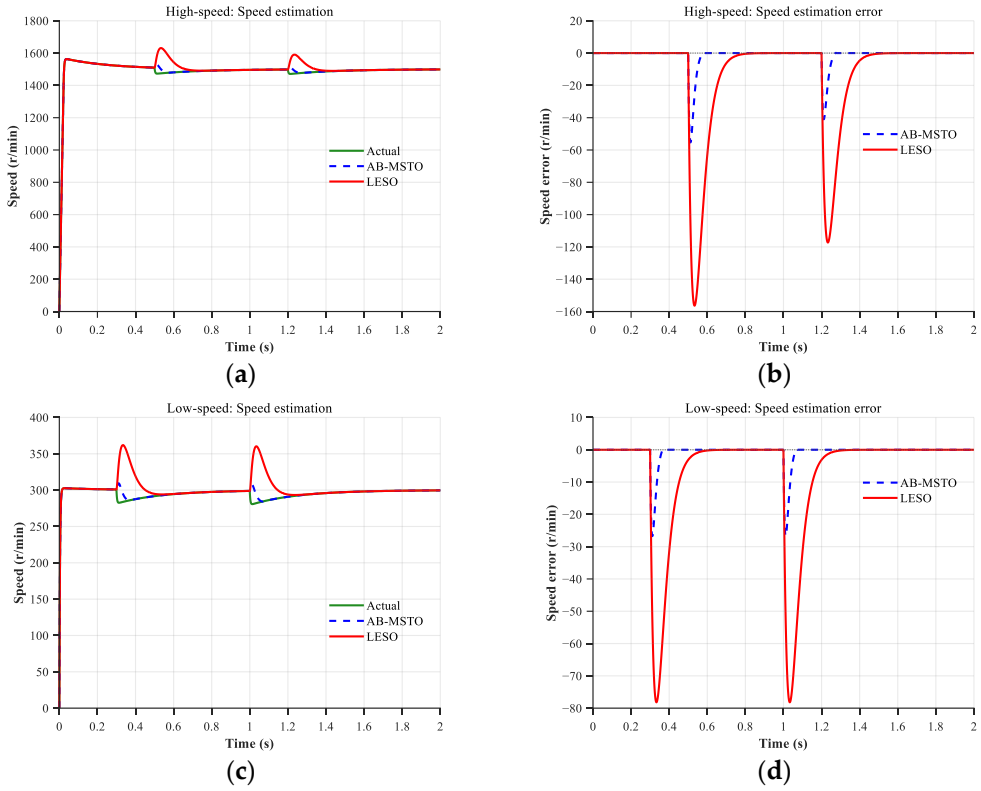


Figure 7. Estimation performance of AB-MSTO and LESO under different SRM operating conditions: (**a**) High-speed: Speed estimation; (**b**) High-speed: Speed estimation error; (**c**) Low-speed: Speed estimation; (**d**) Low-speed: Speed estimation error.

The simulation is based on the mechanical dynamic model of a 12/8-pole SRM with a moment of inertia of $J = 0.0015\,\mathrm{kg \cdot m^2}$ and a viscous damping coefficient of $B = 0.002\,\mathrm{N \cdot m \cdot s/rad}$. Two operating conditions are considered. In the high-speed startup condition shown in Figure 7a,b, the reference speed is 1500 r/min (157.08 rad/s); the load torque steps from 0 to 2 N · m at 0.5 s and then to 3.5 N · m at 1.2 s. In the low-speed condition shown in Figure 7c,d, the reference speed is 300 r/min (31.42 rad/s); the load torque steps from 0 to 1 N · m at 0.3 s and then to 2 N · m at 1.0 s. Both observers use the same speed controller.

Figure 7a,c compares the actual speed with the estimated speeds. AB-MSTO tracks the actual speed rapidly during startup and after each load transient, whereas LESO exhibits noticeable lag and overshoot. The estimation errors in Figure 7b,d further quantify this difference. The peak estimation error of AB-MSTO remains below approximately 10 r/min, and the error reconverges within approximately 0.05 s after each load change. In contrast, LESO produces peak errors of approximately 30–40 r/min and requires more than 0.2 s to reconverge.

This improvement originates from the super-twisting correction mechanism of AB-MSTO. In addition to the conventional linear error feedback terms, AB-MSTO introduces the fractional power term $k_1|e_\omega|^{1/2}\mathrm{sgn}(e_\omega)$ and the integral sign-related correction generated by $k_2\mathrm{sgn}(e_\omega)$ into the estimation error dynamics. Under the stated bounded rate disturbance assumption and gain conditions, this structure provides finite-time convergence between load torque jumps and robust rejection of disturbances whose derivatives remain bounded. Arbitrarily high-frequency disturbances with unbounded derivatives are not included in the theoretical claim. By contrast, LESO relies only on linear correction terms and therefore provides asymptotic rather than finite-time convergence.

The proposed AB-MSTO estimates the load torque and rotor speed online without directly measuring the load torque. The super-twisting mechanism accelerates estimation-error convergence, while adaptive bandwidth regulation provides a compromise between noise sensitivity and dynamic performance. Consequently, the observer improves disturbance rejection and is suitable for high-precision SRM speed control applications.

5. Simulation Analysis

As shown in the following figure, the optimized SRM control system proposed in this paper consists of an improved nonsingular fast terminal sliding mode speed controller and an adaptive bandwidth modified super-twisting observer. To evaluate the control performance of the proposed strategy, a three-phase 12/8-pole SRM simulation model is built in MATLAB/Simulink, where the motor parameters are obtained from Ansys electromagnetic simulations. To highlight the advantages of the proposed improved strategy, four groups of dynamic load and dynamic speed tests are conducted. The improved strategy is compared with the conventional linear baseline PID controller, which is most commonly used in engineering practice, and with the representative modern second-order super-twisting sliding mode control strategy, which features strong disturbance rejection and low chattering. Figure 8 presents the overall block diagram of the INFTSMC and AB-MSTO.

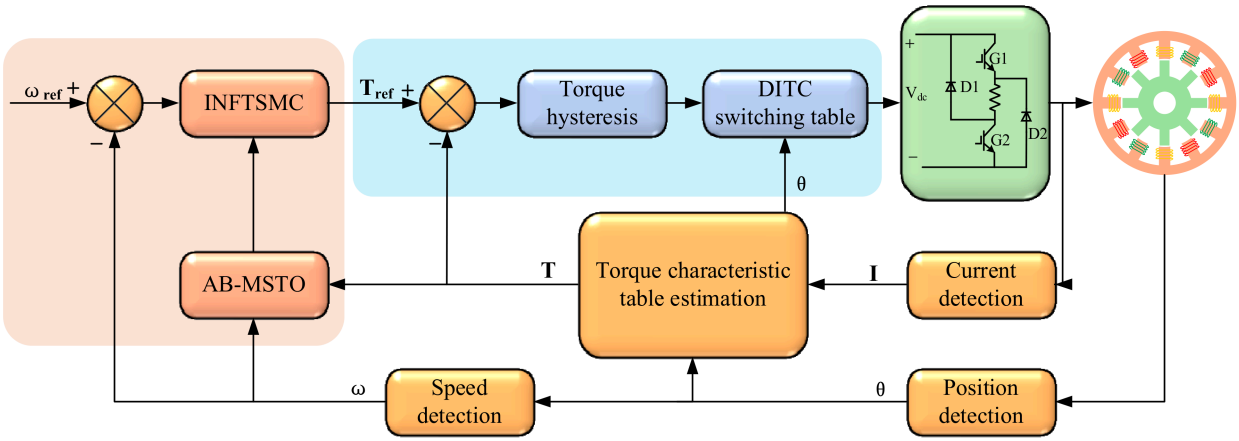


Figure 8. Overall block diagram of the INFTSMC and AB-MSTO.

All comparative simulations were conducted in MATLAB/Simulink using the same SRM model, converter model, and nominal motor parameters reported in the preceding section. The variable step ode45 (Dormand–Prince) solver was employed with a relative tolerance of 10^{-3}, and the simulation duration was set to 1.1 s. A constant numerical increment of $T_s = 1 \times 10^{-6}$ s was used in the discrete accumulation and controller calculations. This value represents the internal algorithmic increment rather than the step size of the variable-step solver.

To ensure a fair and reproducible comparison, PID, STSMC, and INFTSMC were evaluated using identical reference speed commands, load torque profiles, initial conditions, evaluation conditions, DITC logic, DC link power supply, asymmetric bridge power converter, and motor model settings. A common torque command saturation range of $[-40, 40]$·N·m was applied to all compared controllers so that no method could obtain improved performance by using a larger control input. No additional controller-dependent voltage or current limits were imposed beyond the common converter and motor model settings. Once determined, the parameter set of each controller was fixed and used without modification in all operating cases.

The key parameters of the motor model used in the simulation are listed in Table 1.

Table 1. Main parameters of the motor model.

Parameters	Value	Parameters	Value
Number of stator/rotor poles	12/8	Stator inner diameter	216.5 mm
Stator pole arc coefficient	0.42	Stator outer diameter	378 mm
Rotor pole arc coefficient	0.35	Rotor inner diameter	60 mm
Number of winding phases	3	Rotor outer diameter	215.5 mm
Rotor yoke height	27 mm	Stator yoke height	20 mm

The nominal mechanical, electrical, and geometric parameters of the SRM used in the simulation are summarized in Table 1. The geometric dimensions, winding data, material properties, and rated operating quantities were obtained from the design specifications of the investigated SRM. The phase resistance and rotor inertia were determined from the winding and mechanical design data, respectively. The same motor parameters were used for all comparative simulations to ensure a fair evaluation of the different control strategies.

For the PID baseline, the gains were determined through coarse-to-fine iterative tuning under the same SRM model, operating conditions, and physical constraints. Nonzero derivative gains were also tested, but they increased sensitivity to high-frequency speed feedback components without consistently improving the transient response. Therefore, the best tested performance was obtained at $K_d = 0$, and the resulting benchmark operates as a PI-type controller. For the STSMC baseline, the gains were first restricted by the corresponding stability conditions and then refined using the same coarse-to-fine tuning procedure adopted for the PID controller. The final parameters were selected by balancing overshoot, settling and recovery times, tracking accuracy, disturbance rejection, and numerical chattering and were fixed for all comparative simulations. Therefore, the PID and STSMC parameters in Table 2 were not selected through a single arbitrary trial but represent the best overall performance obtained among the tested parameter combinations under identical operating conditions and constraints. No mathematically proven global optimality is claimed.

The controller and observer parameters and their tuning information are summarized in Table 2. The parameters of each method were first selected according to its corresponding control structure and admissible design conditions and were subsequently adjusted under the same simulation environment and common torque command constraint. Once determined, the same parameter set was used in all operating cases. For the AB-MSTO, the adaptive bandwidth sigmoid slope was calculated as ks = 6/eth, rather than tuned independently, and the observer gains were generated online from the scheduled bandwidth.

To ensure a fair and reproducible comparison, the PID and STSMC baseline controllers were independently tuned through an extensive coarse-to-fine iterative procedure before the comparative simulations were conducted. All candidate parameter sets were evaluated using the same nonlinear SRM model, converter configuration, sampling period, current and torque command limits, reference speed profiles, and load disturbance conditions. The tuning process covered startup, reference speed changes, load application, and load removal. Parameter combinations producing instability, sustained oscillation, excessive current, pronounced chattering, or controller output saturation were excluded. Among the remaining candidates, zero or negligible speed overshoot was imposed as the primary tuning requirement, after which the parameter sets providing the shortest settling and recovery times, the smallest tracking error, and the smoothest control response were retained. The final PID and STSMC parameters listed in Table 2 therefore represent the best overall performance obtained among the extensively tested parameter combinations under the common simulation conditions and physical constraints. Once selected, these parameters were fixed and used without further case-dependent adjustment in all operating scenar-

ios. The term "best" here refers to the best compromise obtained within the investigated parameter ranges and does not imply a mathematically proven global optimum.

Table 2. Parameters and tuning information of the compared controllers and observer.

Method	Parameters and Implementation Settings	Tuning Information
PID	K_p = 0.13; K_i = 2.8; K_d = 0; continuous-time parallel structure.	The derivative channel was disabled to avoid additional sensitivity to high-frequency components in the speed feedback signal. The gains were adjusted under the common model and torque constraint to obtain stable tracking without sustained oscillation.
STSMC	c = 120; c_1 = 1.3; fractional exponent = 1/2; smooth switching function $2/[1 + \exp(-e)] - 1 = \tanh(e/2)$.	The gains were adjusted under the same model and torque constraint. The smooth switching function was adopted to reduce numerical chattering.
INFTSMC	T_f, base = 0.024 s; Δ = 0.18 rad/s; p_{pow}/q_{pow} = 1/2; δ_{fs}= 0.20; p_{gain} = 540; q_{gain} = 350; λ_0 = 0.12; λ_1 = 0.10; e_0 = 80 r/min.	The parameters were selected according to the fixed-time design conditions and subsequently adjusted under the common simulation and torque constraints.
AB-MSTO	ω_{far} = 420 rad/s; ω_{near} = 220 rad/s; eth = 30 r/min (3.142 rad/s); $k_s = 6/\text{eth} \approx 1.91$ s/rad; ξ = 1.05; τ_L = 0.50 s; leakage coefficient $\gamma_L = 0.02/\tau_L = 0.04\ s^{-1}$; estimated load-torque limit = [−100, 100] N·m; explicit Euler discretization; $T_s\omega_o \leq 0.1$.	The near- and far-region bandwidths were selected to balance transient response and noise sensitivity. The gains l1, l2, k1, and k2 were calculated online from the scheduled bandwidth according to the gain relationships presented in Section 4. The leakage and projection terms were used to suppress estimator drift and prevent unbounded load-torque estimates.

To further quantify the speed regulation accuracy and disturbance rejection performance, the maximum absolute speed error is defined as

$$E_{\omega,\max} = \max_{t\in[t_a,t_b]}\left|\omega_{ref}(t) - \omega(t)\right|, \tag{46}$$

where $\omega_{ref}(t)$ and $\omega(t)$ denote the reference speed and actual motor speed, respectively, and $[t_a, t_b]$ is the selected evaluation interval. For the start-up condition, $E_{\omega,max}$ is evaluated over the selected steady-state interval after the motor speed has settled. For the load torque step conditions, it is evaluated over the corresponding transient interval beginning at the instant of the load change. The same evaluation intervals are used for all compared controllers.

To quantitatively evaluate the speed fluctuation of the SRM under different operating conditions, the speed ripple ratio is defined as

$$\delta_\omega = \frac{|\omega_{\max} - \omega_{\min}|}{\omega_m} \times 100\% \tag{47}$$

where ω_{max}, ω_{min}, and ω_m denote the maximum, minimum, and average values of the motor speed within the selected steady-state evaluation interval, respectively.

On the other hand, in steady-state performance analysis of motors, torque ripple is an important indicator of output smoothness. The torque ripple coefficient can be used to quantitatively evaluate the simulated torque results [24], and it is defined as

$$K_T = \frac{T_{max} - T_{min}}{T_{avg}} \times 100\% \tag{48}$$

where T_{max}, T_{min}, and T_{avg} are the maximum, minimum, and average values of the torque ripple, respectively.

The recovery time t_r is defined as the elapsed time from the instant t_0 at which a load torque or reference speed change occurs to the earliest instant t_s at which the motor speed enters and subsequently remains within a ±2% settling band around the corresponding steady-state reference speed. Accordingly,

$$t_r = t_s - t_c \tag{49}$$

where t_s satisfies

$$|\omega(t) - \omega_{ref}| \leq 0.02|\omega_{ref}|, \quad t \in [t_s, t_f], \tag{50}$$

and t_f denotes the end of the evaluated transient interval. The same settling band criterion was applied to all compared controllers and operating cases.

No artificial measurement noise or motor parameter perturbation was introduced in the present benchmark simulations. Therefore, all controllers were compared under the same nominal measurement and parameter conditions, while disturbance rejection performance was evaluated through the specified load torque and reference speed changes. Four common operating cases were applied identically to all compared controllers. In the first case, the SRM operated at 1000 r/min, and the load torque was increased from 5 to 9 N·m. In the second case, the SRM operated at 500 r/min, and the load torque was first increased from 5 to 9 N·m and subsequently reduced to 4 N·m. In the third case, the SRM started under a load torque of 9 N·m, while the reference speed was increased from 400 to 1000 r/min. In the fourth case, the same reference speed step was applied under a load torque of 4 N·m. Identical reference commands and load torque profiles were used for PID, STSMC, and INFTSMC.

5.1. Performance Comparison of Dynamic Load Tests Under High-Speed Starting Conditions

Figures 9 and 10 present the time-domain waveforms of speed and electromagnetic torque for three control schemes when the SRM starts at a rated speed of 1000 r/min, with the load torque stepping from an initial 5 N·m to 9 N·m and then being adjusted to 4 N·m. The results are summarized in Table 3.

Table 3. Quantitative comparison of transient and steady-state performance among different control algorithms under high-speed starting and dynamic load conditions.

	PID	STSMC	INFTSMC
Recovery time during start-up (s)	0.0385	0.0679	0.0192
Recovery time during the torque step to 9 N·m (s)	0.352	0.0283	0.0012
Speed ripple ratio during the torque step to 9 N·m (%)	3.65	0.770	0.0509
Recovery time during the torque step to 4 N·m (s)	0.443	0.0615	0.00414
Speed ripple ratio during the torque step to 4 N·m (%)	4.52	1.18	0.218
Torque ripple coefficient (%)	5.39	5.65	3.05
Maximum steady-state speed error after start-up (r/min)	0.095	0.056	0.006
Maximum speed deviation during the load torque step from 5 to 9 N·m (r/min)	36.519	7.709	0.509
Maximum speed deviation during the load torque step from 9 to 4 N·m (r/min)	45.223	11.830	2.182

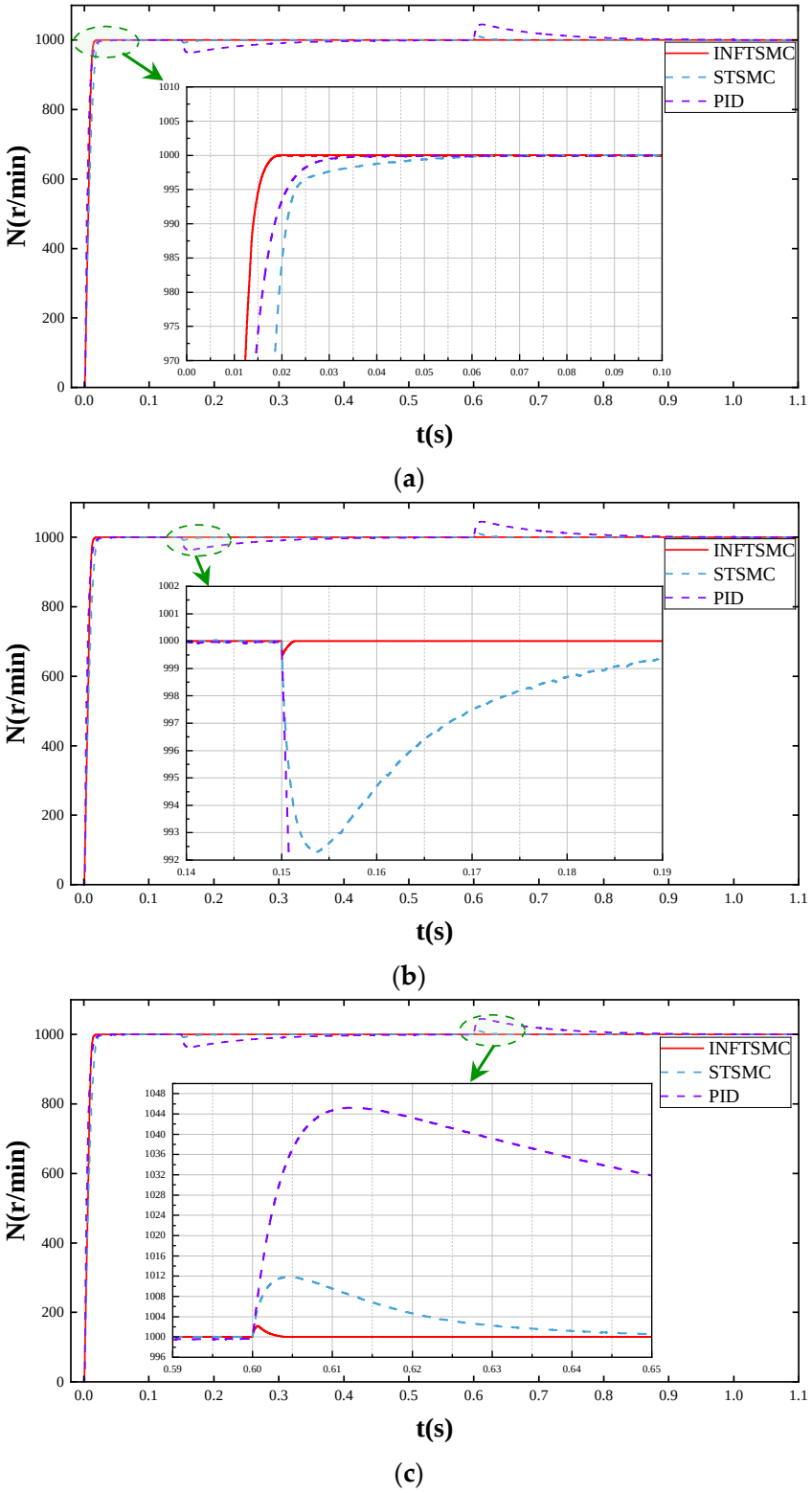


Figure 9. Speed–time curves under high-speed startup and dynamic load conditions: (**a**) start-up instant; (**b**) instant when the load torque suddenly increases; (**c**) instant when the load torque suddenly decreases.

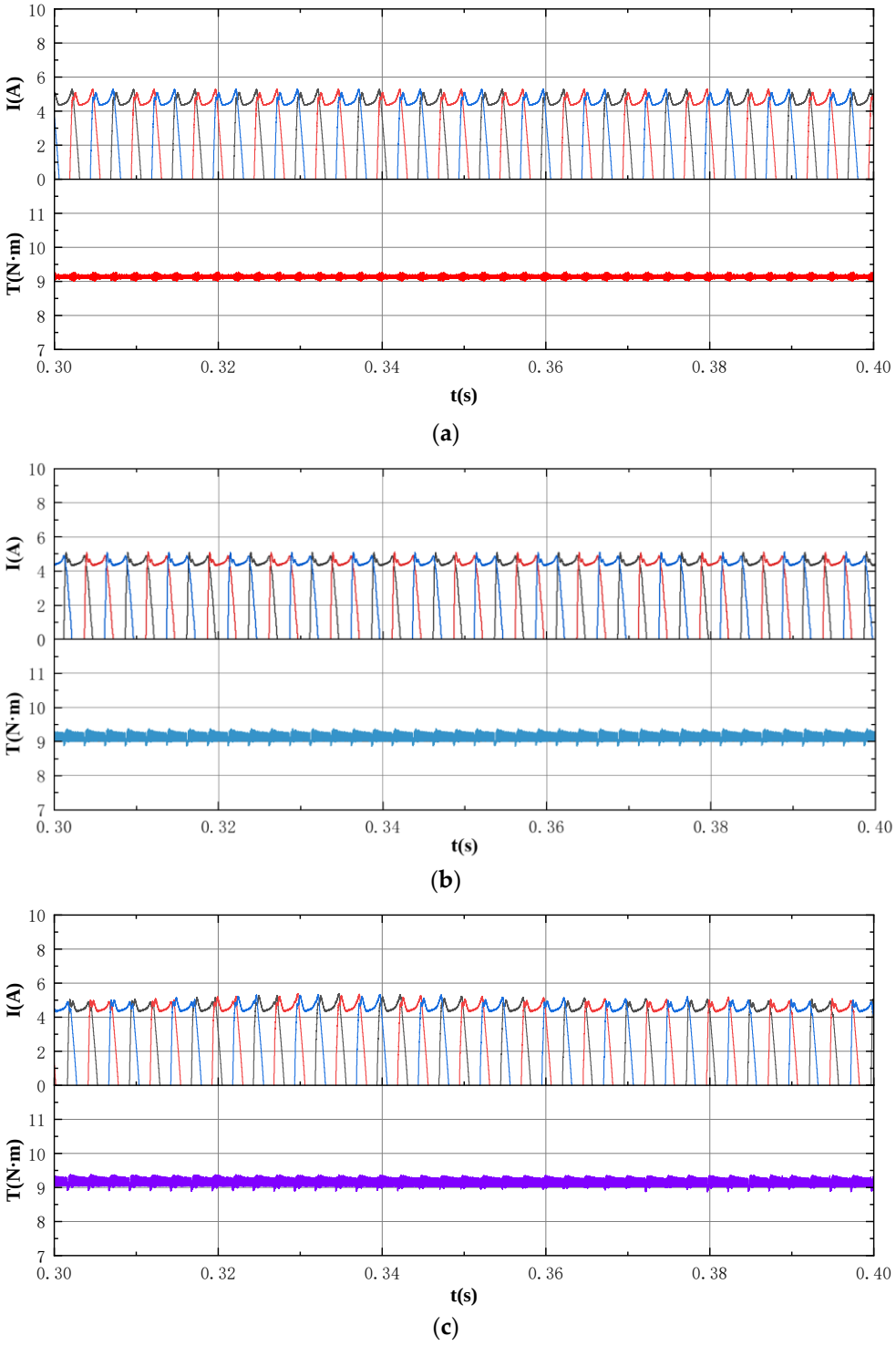


Figure 10. Waveform diagrams of torque and current versus time for three control algorithms under high-speed startup and dynamic load: (**a**) INFTSMC, (**b**) STSMC, and (**c**) PID. In each subfigure, the upper part shows the three-phase current waveforms (black, red, yellow, and blue for phases a, b, and c, respectively), and the lower part shows the torque waveform.

As can be seen from Figure 10, the electromagnetic torque under PID control and super-twisting control fluctuates within approximately 9.37–8.88 N·m and 9.38–8.87 N·m, respectively, whereas the proposed improved strategy significantly narrows the torque fluctuation range to 9.28–9.00 N·m. Here and throughout this paper, the two values in each torque fluctuation range are reported in the order of the maximum value followed by the minimum value.

5.2. Performance Comparison of Dynamic Load Tests Under Low-Speed Starting Conditions

Figures 11 and 12 present the time-domain waveforms of speed and electromagnetic torque for three control schemes when the SRM starts at a rated speed of 500 r/min, with the load torque stepping from an initial 5 N·m to 9 N·m and then being adjusted to 4 N·m. The results are summarized in Table 4.

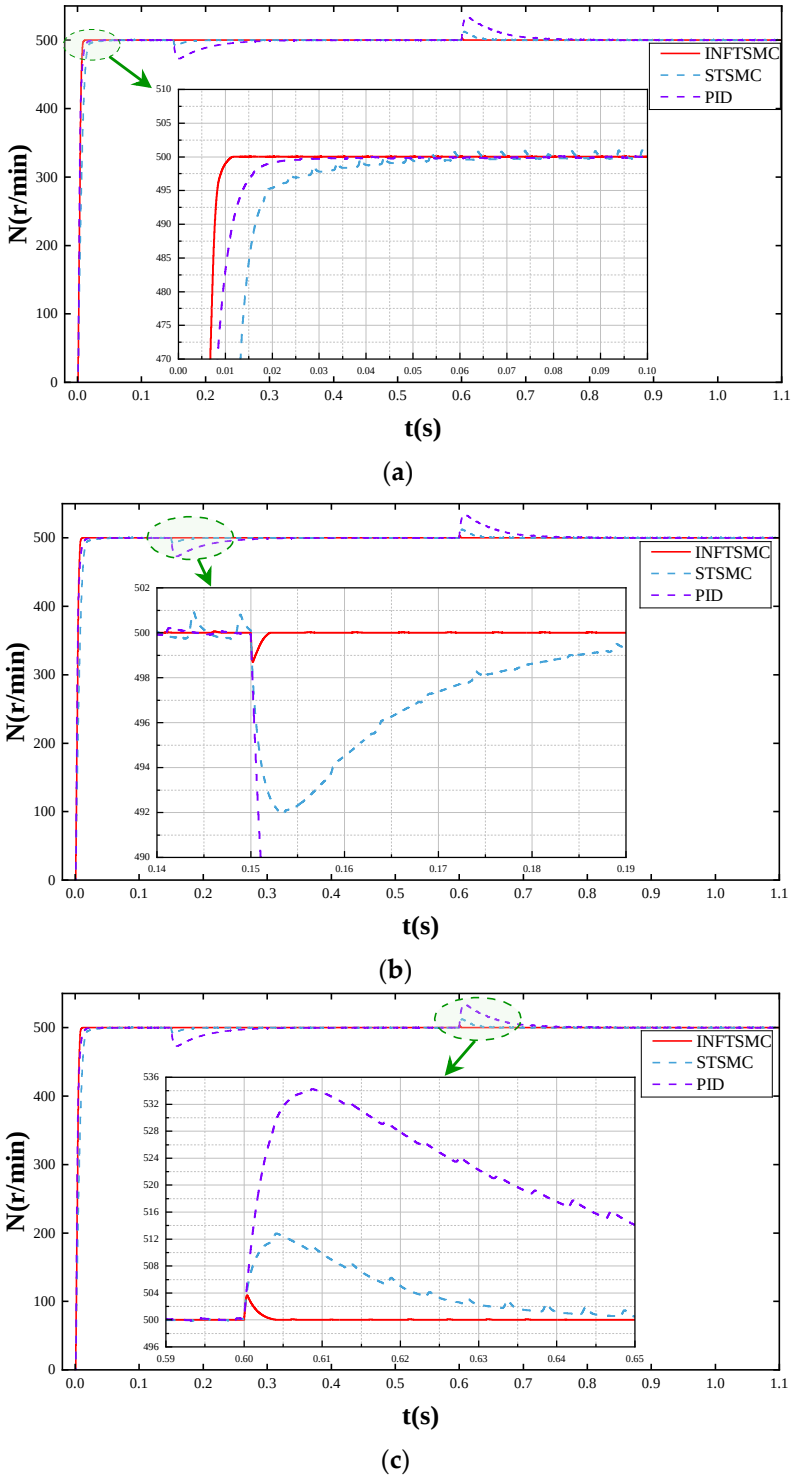


Figure 11. Speed–time curves under low-speed startup and dynamic load conditions: (**a**) start-up instant; (**b**) instant when the load torque suddenly increases; (**c**) instant when the load torque suddenly decreases.

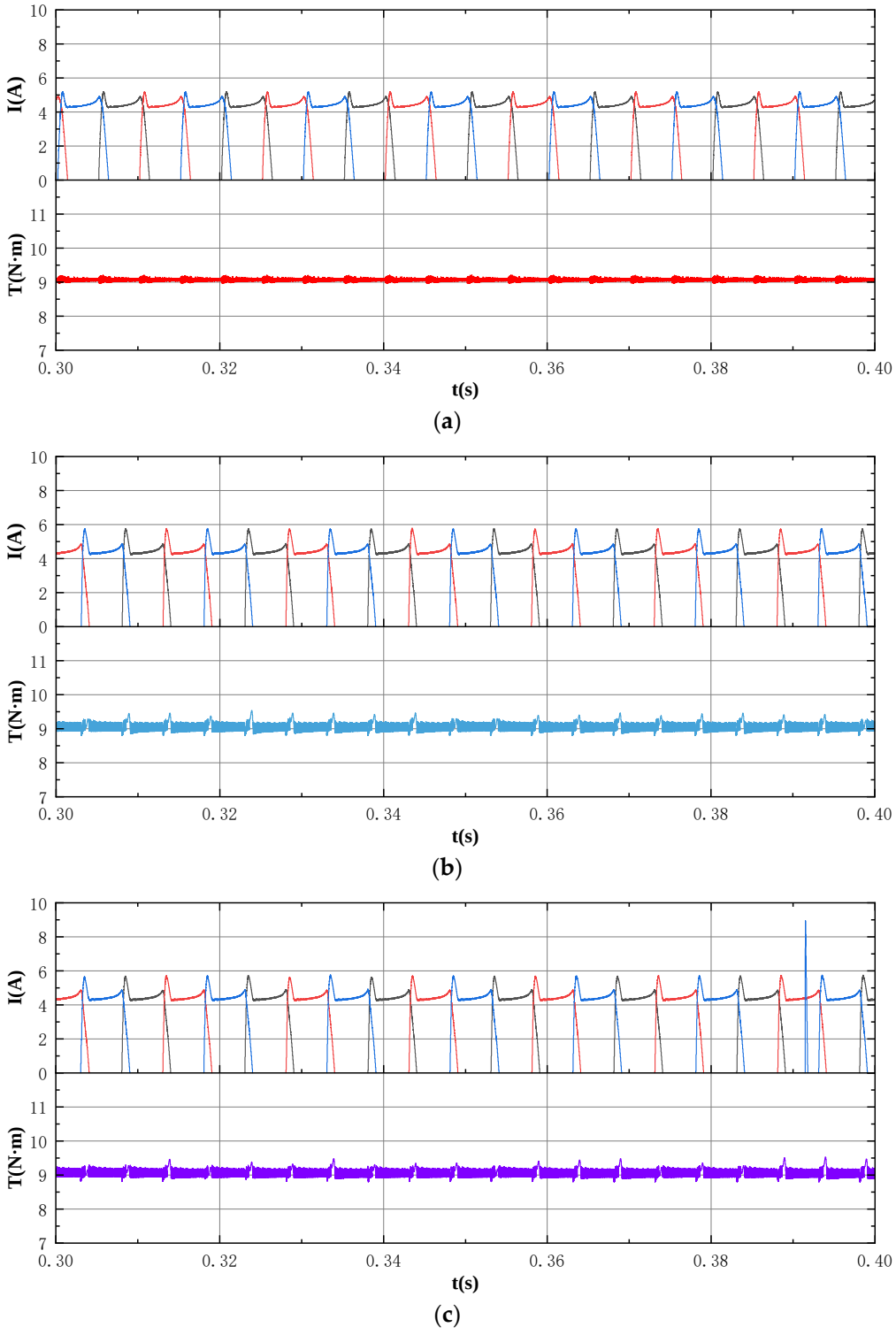


Figure 12. Waveform diagrams of torque and current versus time for three control algorithms under low-speed startup and dynamic load: (**a**) INFTSMC, (**b**) STSMC, and (**c**) PID. In each subfigure, the upper part shows the three-phase current waveforms (black, red, yellow, and blue for phases a, b, and c, respectively), and the lower part shows the torque waveform.

As can be seen from Figure 12, the electromagnetic torque under PID control and super-twisting control fluctuates within approximately 9.5005–8.7951 N·m and 9.5401–8.791 N·m, respectively, whereas the proposed improved strategy significantly narrows the torque fluctuation range to 9.208–8.969 N·m.

Table 4. Quantitative comparison of transient and steady-state performance among different control algorithms under low-Speed starting and dynamic load conditions.

	PID	STSMC	INFTSMC
Recovery time during start-up (s)	0.0312	0.0435	0.0115
Recovery time during the torque step to 9 N·m (s)	0.151	0.0541	0.0021
Speed ripple ratio during the torque step to 9 N·m (%)	5.40	1.61	0.26
Recovery time during the torque step to 4 N·m (s)	0.0261	0.0631	0.00446
Speed ripple ratio during the torque step to 4 N·m (%)	6.85	2.57	0.731
Torque ripple coefficient (%)	7.71	8.17	2.63
Maximum steady-state speed error after start-up (r/min)	0.323	0.989	0.078
Maximum speed deviation during the load torque step from 5 to 9 N·m (r/min)	26.988	8.036	1.305
Maximum speed deviation during the load torque step from 9 to 4 N·m (r/min)	34.265	12.839	3.657

5.3. Performance Comparison of Dynamic Speed Tests Under High-Torque Starting Conditions

Figure 13 shows the speed–time waveforms of the three control schemes when the SRM starts under a load torque of 9 N·m and the rated speed steps from 400 r/min to 1000 r/min. The performance of different controllers is quantitatively evaluated in terms of maximum speed deviation, recovery time, and steady-state speed error. The results are summarized in Table 5.

Table 5. Quantitative comparison of transient and steady-state performance among different control algorithms under high-torque starting and dynamic speed conditions.

	PID	STSMC	INFTSMC
Recovery time during start-up (s)	0.1052	0.1061	0.0122
Recovery time during the speed step to 1000 r/min (s)	0.242	0.0495	0.0122
Speed ripple ratio during the speed step to 1000 r/min (%)	5.53	0.169	0.002
Maximum steady-state speed error after start-up at 400 r/min (r/min)	0.801	0.215	0.112
Maximum speed deviation during the speed step from 400 to 1000 r/min (r/min)	55.287	1.687	0.02
Maximum steady-state speed error after the speed step to 1000 r/min (r/min)	0.0685	0.0622	0.0062

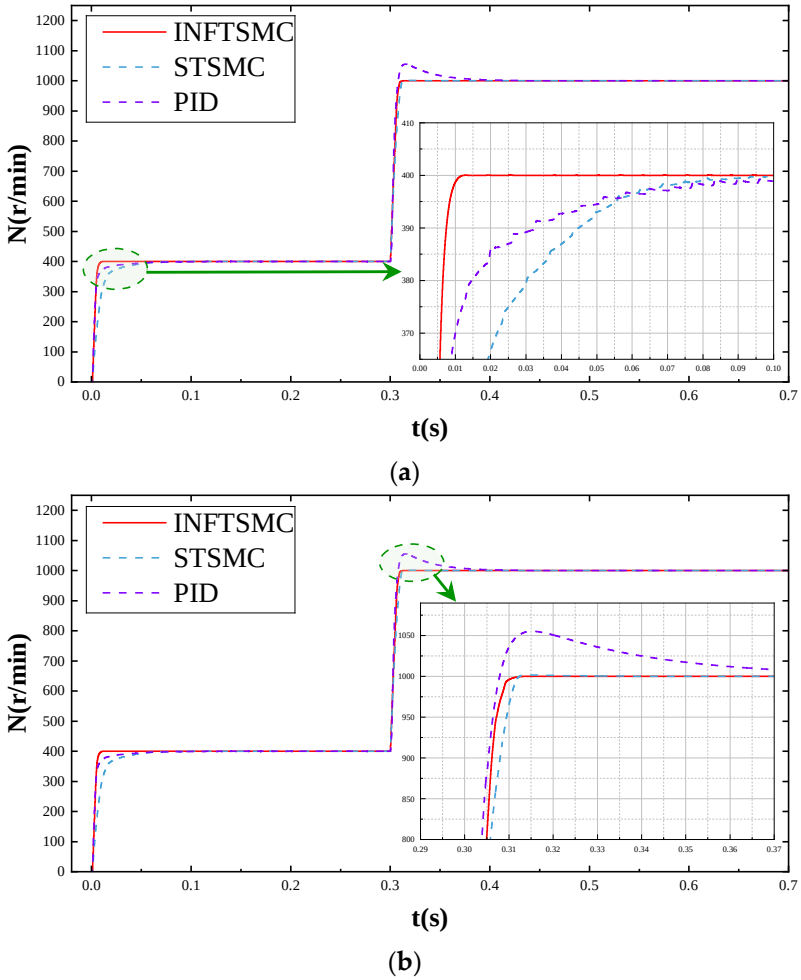


Figure 13. Speed–time curve under high torque and dynamic speed conditions: (**a**) start-up instant; (**b**) when the speed command suddenly increases.

5.4. Performance Comparison of Dynamic Speed Tests Under Low-Torque Starting Conditions

Figure 14 shows the speed–time waveforms of the three control schemes when the SRM starts under a load torque of 4 N·m and the rated speed steps from 400 r/min to 1000 r/min. The performance of different controllers is quantitatively evaluated in terms of maximum speed deviation, recovery time, and steady-state speed error. The results are summarized in Table 6.

Table 6. Quantitative comparison of transient and steady-state performance among different control algorithms under low-torque starting and dynamic speed conditions.

	PID	STSMC	INFTSMC
Recovery time during start-up (s)	0.0188	0.0335	0.0101
Recovery time during the speed step to 1000 r/min (s)	0.266	0.0462	0.0124
Speed ripple ratio during the speed step to 1000 r/min (%)	3.43	0.169	0.008
Maximum steady-state speed error after start-up at 400 r/min (r/min)	1.865	1.801	0.551

Table 6. *Cont.*

	PID	STSMC	INFTSMC
Maximum speed deviation during the speed step from 400 to 1000 r/min (r/min)	34.317	1.689	0.081
Maximum steady-state speed error after the speed step to 1000 r/min (r/min)	0.046	0.055	0.005

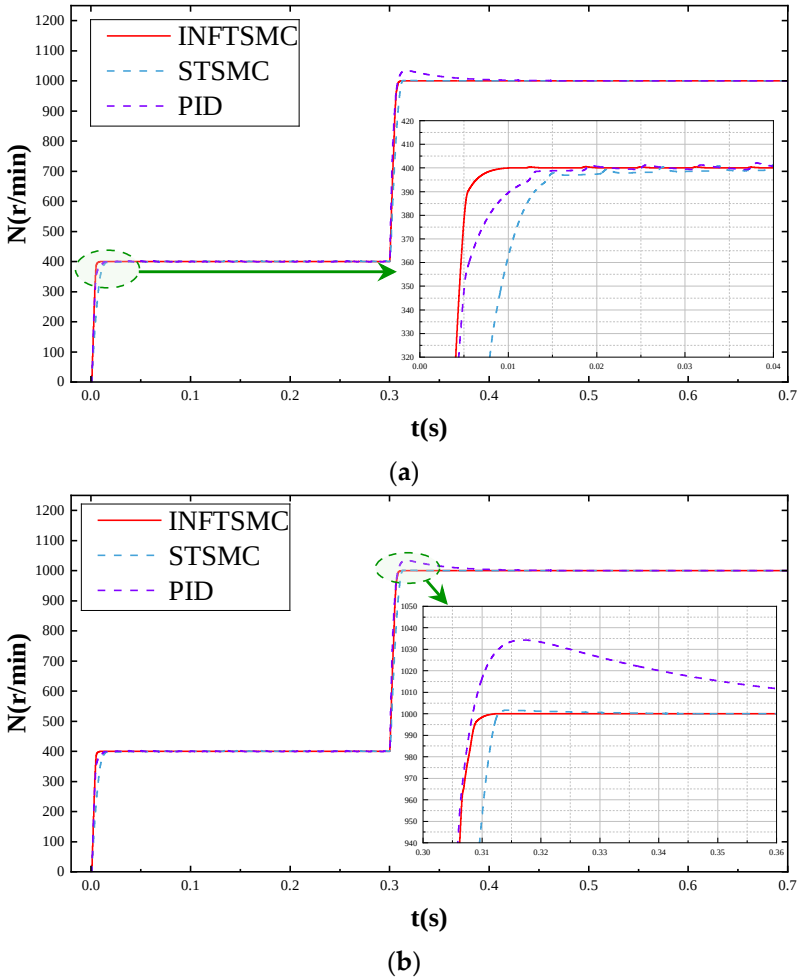


Figure 14. Speed–time curve under low torque and dynamic speed conditions: (**a**) start-up instant; (**b**) when the speed command suddenly increases.

The above simulation results demonstrate the comparative control performance of the proposed INFTSMC under the specified MATLAB/Simulink conditions. The control law involves hyperbolic tangent functions, fractional power operations, and piecewise interpolation. Its actual computational requirement depends on the target processor, numerical implementation, compiler optimization, and controller update rate. Quantitative real-time implementation evaluation and hardware-in-the-loop validation will be considered in future work.

6. Conclusions

This paper proposes a high-performance SRM speed regulation scheme integrating INFTSMC with an AB-MSTO and verifies its effectiveness in suppressing torque ripple and reducing speed fluctuations through comparative tests under dynamic disturbances. Compared with PID and STSMC, the proposed strategy reduces the speed ripple ratio

to 0.002% and 0.008% in the dynamic speed tests with high- and low-torque start-up, respectively, whereas the corresponding values are 5.53% and 3.43% for PID and 0.169% in both cases for STSMC. In the dynamic load tests with high- and low-speed start-up, the torque ripple coefficient is reduced by 43.41% and 65.89%, respectively, relative to PID. The speed ripple ratios during the load torque transitions are also substantially reduced, demonstrating the improved dynamic tracking and disturbance rejection performance of the proposed strategy. Mechanistically, INFTSMC achieves fast convergence and smooth control via coordinated far- and near-region actions, avoiding singularity and alleviating chattering; meanwhile, AB-MSTO rapidly estimates and compensates for load disturbances and unmodeled dynamics, enabling the system to maintain strong robustness and superior dynamic response under parameter variations, abrupt load changes, and start-up transients.

Despite the promising simulation results, this work still has some limitations. The proposed INFTSMC and AB-MSTO have been validated only through MATLAB/Simulink simulations based on a high-fidelity nonlinear SRM model. Although the theoretical convergence analysis verifies the feasibility of the proposed method, experimental validation on a DSP/FPGA-based hardware platform is still required to further confirm its real-time implementation capability and practical robustness. At present, the experimental platform construction, including the preparation and integration of the required hardware devices, is being actively carried out for future experimental verification. Furthermore, the parameter tuning of INFTSMC still relies on engineering experience, and systematic auto-tuning strategies remain to be investigated. Future work will focus on experimental implementation, adaptive gain optimization, and extension of the proposed method to more complex servo systems.

Author Contributions: We confirm that all listed authors, namely L.Z., C.L., J.Z. and R.L., made substantial contributions according to the CRediT taxonomy, with specific roles as follows: L.Z. was responsible for conceptualization, methodology, formal analysis, and writing—original draft; C.L. for software, data curation, validation, and writing—review and editing; J.Z. for supervision, resources, and writing—review and editing; R.L. for supervision, project administration, and writing—review and editing. Furthermore, no additional contributors have been omitted, and all acknowledged individuals have given their permission. All authors have read and agreed to the published version of the manuscript.

Funding: This research was funded by the project "Monitoring, Early Warning and Energy Efficiency Evaluation System for High-power Rectifier Devices" of the Jilin Provincial Development and Reform Commission (2022C045-11) and the graduate student innovation project "Control Strategy for Switched Reluctance Motors in New Energy Vehicles" of Beihua University (YCHZ [2025]014).

Data Availability Statement: The original contributions presented in this study are included in the article. Further inquiries can be directed to the corresponding author.

Conflicts of Interest: The authors declare no conflicts of interest.

Nomenclature

Abbreviations

Abbreviation	**Full term**
SRM	Switched reluctance motor
DITC	Direct instantaneous torque control
INFTSMC	Improved nonsingular fast terminal sliding mode control
NFTSMC	Nonsingular fast terminal sliding mode control
NFTS	Nonsingular fast terminal sliding surface
STSMC	Super-twisting sliding mode control
AB-MSTO	Adaptive bandwidth modified super-twisting observer

LESO	Linear extended state observer
PID	Proportional–integral–derivative
FEA	Finite element analysis
PWM	Pulse-width modulation
DSP	Digital signal processor
FPGA	Field-programmable gate array
ADRC	Active disturbance rejection control

Symbols

Symbol	**Definition**	**Unit**
T_k	Instantaneous electromagnetic torque generated by the kth phase	N·m
T_e	Total electromagnetic torque generated by the motor	N·m
i_k	Instantaneous current of the kth phase	A
ψ_k	Flux linkage of the kth phase	Wb
θ	Rotor angular position	rad (° for FEA data)
W'_k	Magnetic co-energy of the kth phase	J
W_k	Magnetic field energy of the kth phase	J
ι	Dummy current variable used for integration	A
k	Phase index	—
m	Number of motor phases	—
J	Moment of inertia	$kg{\cdot}m^2$
B	Viscous friction coefficient	N·m·s/rad
T_L	Load torque	N·m
ω	Actual rotor angular speed	rad/s
ω_{ref}	Reference rotor angular speed	rad/s
$\dot{\omega}_{ref}$	Time derivative of the reference rotor angular speed	rad/s^2
E_ω	Speed tracking error, defined as the difference between the reference and actual rotor speeds	rad/s
s	Sliding variable	—
a_1, a_2	Positive gains of the improved integral sliding surface	—
$\lambda(E_\omega)$	Adaptive power exponent function	—
λ_0, λ_1	Positive adaptive coefficients	—
e_0	Positive scaling factor for the speed tracking error	rad/s
k_r	Reaching gain of the conventional smooth reaching law	—
φ	Boundary layer thickness of the conventional smooth reaching law	Same as s
c_0	Integral gain of the conventional sliding surface	—
k_1, k_2	Positive gains of the improved double-power reaching law	—
α, β	Power exponents of the conventional double-power reaching law	—
p, q	Positive integers defining the fractional exponent p/q	—
c	Positive damping gain of the improved reaching law	—
Δ	Boundary layer thickness of the hyperbolic tangent function	Same as s
$H(s)$	Continuous interpolation function connecting the fractional- and quadratic power terms	—
$\alpha(s)$	Continuous weighting function in the interpolation region	—
δ	Half-width of the interpolation interval	—
T_f	Gain scaling parameter associated with the practical convergence time bound	s
V	Lyapunov function of the sliding variable dynamics	—
x	Absolute value of the sliding variable	—
ε	Radius of the prescribed convergence neighborhood	Same as s
T_1	Upper bound of the far-region convergence time	s

T_2	Upper bound of the near-region convergence time	s
T_ε	Total practical convergence time bound	s
C_ε	Coefficient relating the gain scaling parameter to the practical convergence time bound	—
T_d	Prescribed practical convergence time	s
b(x)	Input coefficient of the SRM speed dynamics	—
b_{min}, b_{max}	Lower and upper bounds of the input coefficient	—
T_{ref}	Reference electromagnetic torque command generated by the speed controller	N·m
T_{eq}	Equivalent control torque	N·m
T_{sw}	Switching control torque	N·m
x_1	Extended state representing the rotor angular speed	rad/s
x_2	Extended state representing the load torque	N·m
T_{ctrl}	Actual torque command applied to the SRM after torque saturation	N·m
$\hat{\omega}$	Estimated rotor angular speed	rad/s
$\hat{T}_L$	Estimated load torque	N·m
e_ω	Speed estimation error, defined as the difference between the actual and estimated rotor speeds	rad/s
$\tilde{T}_L$	Difference between the actual and estimated load torques	N·m
l_1, l_2	Linear observer gains	—
g_1, g_2	Nonlinear super-twisting correction gains	—
ξ	Super-twisting strength coefficient	—
$\omega_0(e_\omega)$	Adaptive observer bandwidth determined by the speed estimation error	rad/s
ω_{near}	Observer bandwidth in the near-origin region	rad/s
ω_{far}	Observer bandwidth in the far-error region	rad/s
$S(\lvert e_\omega \rvert, eth)$	Smooth bandwidth switching function	—
eth	Prescribed speed estimation error threshold	rad/s
k_s	Switching slope coefficient determining the bandwidth transition steepness	—
v	Transformed load torque estimation error	rad/s^2
d(t)	Normalized disturbance associated with the load torque derivative	rad/s^3
$\overline{D}$	Upper bound of the load torque derivative	N·m/s
D	Upper bound of the normalized disturbance	rad/s^3
a	Combined linear coefficient of the transformed observer error dynamics	s^{-1}
λ_0	Fractional power correction coefficient of the transformed observer error system	—
α_0	Sign-related correction coefficient of the transformed observer error system	—
β_0	Linear correction coefficient of the transformed observer error system	—
$\lambda_{0,min}$, $\lambda_{0,max}$	Lower and upper bounds of the fractional power correction coefficient	—
$\alpha_{0,min}$, $\alpha_{0,max}$	Lower and upper bounds of the sign-related correction coefficient	—
z_1, z_2	Transformed observer error variables	—
z	Transformed observer error vector	—
μ	Bounded uncertainty parameter in the matrix representation	—
A	State matrix of the transformed observer error system	—
P	Common symmetric positive definite Lyapunov matrix	—

Q	Symmetric positive definite matrix in the Lyapunov inequality	—
V_0	Lyapunov function of the observer error system	—
c_0	Positive convergence coefficient in the Lyapunov inequality	—
t_0	Initial time of the considered continuous disturbance interval	s
T_0	Finite convergence time of the observer errors	s
$E_{\omega,max}$	Maximum absolute speed error	Same as ω
t	Time variable	s
t_a, t_b	Starting and ending times of the selected evaluation interval	s
δ_ω	Speed ripple ratio	%
ω_{max}	Maximum motor speed within the selected evaluation interval	Same as ω
ω_{min}	Minimum motor speed within the selected evaluation interval	Same as ω
ω_m	Average motor speed within the selected evaluation interval	Same as ω
K_T	Torque ripple coefficient	%
T_{max}	Maximum electromagnetic torque within the evaluation interval	N·m
T_{min}	Minimum electromagnetic torque within the evaluation interval	N·m
T_{avg}	Average electromagnetic torque within the evaluation interval	N·m
t_r	Recovery time	s
t_c	Instant at which the load torque or reference speed changes	s
t_s	Earliest time at which the motor speed enters and remains within the prescribed settling band	s
t_f	End of the evaluated transient interval	s

References

1. Li, S.; Huang, X.; He, Z.; Liu, Y.; Qu, H.; Wu, J. Multi-mode operations of double-stator switched reluctance machine for electric vehicle. *COMPEL-Int. J. Comput. Math. Electr. Electron. Eng.* **2024**, *43*, 390–413. [CrossRef]
2. Ge, L.; Du, N.; Song, J.; Zhang, J.; Fan, Z.; Zhang, D.; Song, S. Advanced technology of switched reluctance machines in more electric aircraft: A review. *IEEE Trans. Power Electron.* **2024**, *40*, 195–216.
3. Madonna, V.; Meano, C.M.; Hansen, K.F. Performance Improvement of Switched Reluctance Machines Through Appropriate Design Choices. In Proceedings of the 2025 IEEE Workshop on Electrical Machines Design, Control and Diagnosis (WEMDCD), Valletta, Malta, 9–10 April 2025; pp. 1–7.
4. Ge, L.; Fan, Z.; Zhang, J.; Sun, G.; Liu, S.; Xiao, D.; Song, S. A Novel Torque Ripple Suppression Method for Switched Reluctance Machine Based on Piecewise Linear Flux-Linkage Profile. *IEEE Trans. Ind. Electron.* **2024**, *72*, 6547–6552.
5. Malekpour, H.; Rashidi, A.; Nejad, S.M.S.; Lee, D.H. Multi-Level Voltage High Fault-Tolerance Modular SRM Converter with Simultaneous Charge and Discharge Capability for HEV. *IEEE Access* **2025**, *13*, 127447–127461. [CrossRef]
6. Yedukondalu, R.; Chandra, B.M.; Rao, R.S. Optimal Control Architecture for Rotor Position Estimation and Torque Ripple Minimization in 8/6 Switched Reluctance Motor. *Optim. Control. Appl. Methods* **2025**, *47*, 166–182. [CrossRef]
7. Boumaalif, Y.; Ouadi, H.; Giri, F. Multi-stage adaptive speed control with torque ripple optimization for a switched reluctance motor in electric vehicle applications. *Results Eng.* **2025**, *25*, 104245.
8. Wang, X.; Wang, X.; Huang, Z.; Wang, B.; Yang, R. Integrated Control Strategy of Bearingless Switched Reluctance Motor Based on Active Disturbance Rejection Control. *IEEE Trans. Ind. Electron.* **2025**, *72*, 7320–7328. [CrossRef]
9. Chen, Z.; Lin, X.; Zhang, S.; Ji, H.; Shen, Y.; Ge, L.; Xiao, D. Autoswitching ADRC-Based Approach for Enhanced Speed Control and Torque Ripple Minimization in Switched Reluctance Motors. *IEEE Trans. Ind. Electron.* **2025**, *72*, 9953–9963. [CrossRef]
10. Ge, L.; Guo, J.; Gong, C.; Zhang, G.; Ding, X.; Song, S. Model predictive torque control of switched reluctance machines with torque sharing function and PWM control signals based on linear polynomial fitting. *IEEE Trans. Power Electron.* **2024**, *40*, 40–45.
11. Zhao, Y.; Zhu, J.; Ren, P.; Cao, H.; Zhang, S. Position-Sensorless Control of SRM Drives Based on a Novel Super-Twisting Sliding Mode Observer with the Machine Learning Model. *IEEE J. Emerg. Sel. Top. Power Electron.* **2025**, *13*, 6178–6189. [CrossRef]
12. Sehab, R.; Akrad, A.; Saadi, Y. Super-twisting sliding mode control to improve performances and robustness of a switched reluctance machine for an electric vehicle drivetrain application. *Energies* **2023**, *16*, 3212. [CrossRef]
13. Li, H.; Li, Z.; Xing, L.; Liang, W.; Chen, X. Direct instantaneous torque control of switched reluctance motor based on improved sliding mode controller and disturbance observer. *Electr. Eng.* **2025**, *107*, 10789–10803. [CrossRef]

14. Guo, X.; Zeng, S.; Zhong, R.; Hua, W. High-Precision Injection Current Sampling Scheme for Direct Drive Low-Speed Position Sensorless Control of Switched Reluctance Machine. *IEEE Trans. Ind. Electron.* **2024**, *71*, 13754–13765. [CrossRef]
15. Moreno, J.A.; Osorio, M. A Lyapunov approach to second-order sliding mode controllers and observers. In Proceedings of the 2008 47th IEEE Conference on Decision and Control, Cancun, Mexico, 9–11 December 2008; pp. 2856–2861.
16. Liu, Y.C.; Laghrouche, S.; Depernet, D.; N'Diaye, A.; Djerdir, A.; Cirrincione, M. Disturbance-observer-based speed control for SPMSM drives using modified super-twisting algorithm and extended state observer. *Asian J. Control.* **2024**, *26*, 1089–1102. [CrossRef]
17. Yang, Q.; Mao, K.; Zheng, S.; Zhou, C.; Zhong, Q. Position sensorless drive with online parameters estimation for magnetic suspension centrifugal compressor. *IEEE Trans. Power Electron.* **2023**, *38*, 9384–9394. [CrossRef]
18. Liu, Y.C. Disturbance-observer-based second-order sliding-mode position control for permanent-magnet synchronous motors: A continuous twisting algorithm-based approach. *Energies* **2024**, *17*, 2974. [CrossRef]
19. He, H.; Yao, X.; Wang, J.; Zheng, B.; Guan, Q. Current Optimized Torque Sharing Function Control for Switched Reluctance Motor Based on Quasi-Proportional Resonance Controller. *IEEE J. Emerg. Sel. Top. Power Electron.* **2024**, *13*, 1662–1672. [CrossRef]
20. Mohanraj, D.; Samithas, D.; Balachandran, P.K.; Zainuri, M.A.A.M. An Improved Power Factor Correction Converter for Switched Reluctance Motor Drive Performance Analysis. *IEEE Access* **2025**, *13*, 71187–71196. [CrossRef]
21. Sreeram, K.; Preetha, P.K.; Javier, R.G.; Carlos, Á.B. A comprehensive review of torque and speed control strategies for switched reluctance motor drives. *CES Trans. Electr. Mach. Syst.* **2025**, *9*, 46–75. [CrossRef]
22. Feng, Y.; Yu, X.; Han, F. On nonsingular terminal sliding-mode control of nonlinear systems. *Automatica* **2013**, *49*, 1715–1722. [CrossRef]
23. Yu, S.; Yu, X.; Shirinzadeh, B.; Man, Z. Continuous finite-time control for robotic manipulators with terminal sliding mode. *Automatica* **2005**, *41*, 1957–1964. [CrossRef]
24. Prestes, G.X.; Moreira, W.K.; Scalcon, F.P.; Rech, C.; Knight, A.M.; Vieira, R.P. Reinforcement Learning-Based Current Controller for Switched Reluctance Motor Drives. In Proceedings of the 2025 IEEE International Electric Machines & Drives Conference (IEMDC), Houston, TX, USA, 18–21 May 2025; pp. 71–76.

Disclaimer/Publisher's Note: The statements, opinions and data contained in all publications are solely those of the individual author(s) and contributor(s) and not of MDPI and/or the editor(s). MDPI and/or the editor(s) disclaim responsibility for any injury to people or property resulting from any ideas, methods, instructions or products referred to in the content.